Journal of Computational Physics 230 (2011) 6916–6957

Contents lists available at ScienceDirect

Journal of Computational Physics

journal homepage: www.elsevier.com/locate/jcp

Numerical implementation of mixing and molecular transport in LES/PDF studies of turbulent reacting flows

Sharadha Viswanathan *, Haifeng Wang, Stephen B. Pope

Sibley School of Mechanical and Aerosapce Engineering, Cornell University, Ithaca, NY 14853, United States

ARTICLE INFO

Article history:
Received 23 September 2010
Received in revised form 7 April 2011
Accepted 16 May 2011
Available online 23 May 2011

Keywords:
LES/PDF methods
Lagrangian Monte Carlo particle methods
IEM mixing model
Molecular diffusion
Differential diffusion
Smoothing

ABSTRACT

Probability Density Function (PDF) methods in combination with Large Eddy Simulations (LES) are a powerful tool for studying turbulent reacting flow problems and we are interested in the implementation of mixing and molecular transport in LES/PDF methods. The numerical methodology used for solution procedure is the hybrid particle/mesh method and a fractional step scheme is used to solve for transport, reaction and mixing sequentially. Mixing is modeled using the Interaction by Exchange with the Mean (IEM) model and the effects of molecular transport are incorporated as a mean drift term in the mixing step. This methodology avoids spurious production of scalar variance and also allows direct incorporation of differential diffusion effects. In this study, various numerical implementations of mixing and molecular transport are presented and evaluated, using the Method of Manufactured Solutions (MMS), for (1) accuracy, (2) detailed conservation, (3) realizability, and (4) stability. Moreover, the methodology is shown to be successful in capturing the effects of differential diffusion accurately with the additional property of ensuring realizability of species mass fractions. Finally and most importantly, we describe a new variance reduction technique by way of an implicit smoothing methodology. This smoothing scheme is shown to satisfy conservation, boundedness and regularity criteria. Moreover, for an appropriate choice of the smoothing length scale, significant improvements in accuracy can be achieved for an incremental increase in computational cost. Also, it is shown that with smoothing on a length scale greater than the grid size, the bias and statistical errors due to there being a finite number of particles in the Lagrangian Monte Carlo simulations scale as N_{tot}^{-1} and $N_{tot}^{-1/2}$ respectively, where N_{tot} is the total number of particles in the computational domain, whereas without smoothing these errors scale as N_{pc}^{-1} and $N_{pc}^{-1/2}$, where N_{pc} is the much smaller number of particles in a computational cell.

1. Introduction

The world's energy needs are primarily satisfied by processes that convert the chemical energy stored in the fossil fuels into usable thermal energy. Given the high depletion rate of fuels as compared to the increasing energy needs of growing economies, there is a strong focus on improving the efficiencies of existing facilities by augmenting their designs. Better understanding of the underlying physics behind the turbulent combustion processes inherent in these systems paves a path to designing better systems.

Turbulent combustion involves several species interacting with each other via multiple chemical reactions and with the underlying turbulent flow. Computational fluid dynamics (CFD) based tools [1] have been used to provide various levels of

* Corresponding author.
E-mail address: sv94@cornell.edu (S. Viswanathan).

0021-9991/$ - see front matter © 2011 Elsevier Inc. All rights reserved.
doi:10.1016/j.jcp.2011.05.020

description to address the turbulence closure problem [2] encountered in the modeling of turbulent reacting flows. Reynolds Averaged Navier Stokes (RANS) based approaches were historically chosen since the computation of instantaneous flow fields in a turbulent reacting flow was not possible. Given the wide range of temporal and spatial scales inherent in a reacting flow calculation, a DNS (Direct Numerical Simulation) gives the most detailed level of description possible by resolving all scales [3]. On the other hand, a LES (Large Eddy Simulation) resolves only the large scales of the turbulent flow while modeling the effects of the small scales [4–6]. In comparison, DNS is still not computationally tractable for high Reynolds number turbulent flow calculations whereas LES is becoming more commonplace with the development and advancement of high performance computing facilities.

In modeling a turbulent reacting flow, the complexity is magnified multi-fold by large density variations and highly non-linear chemical reaction rates. Probability Density Function (PDF) [4,7–9] methods have been proven to be highly successful in addressing most of the closure problems including closure of the non-linear chemical source terms due to reaction. In the context of LES, based on the filtering operation performed, a PDF analogue called the Filtered Density Function (FDF) [8,10–12] is defined. Though there are many variants to the definition of LES, the most dominant approach is based on 'filtering'. Recently, Pope [13] introduced the idea of self-conditioned fields as an alternative to the filtering approach. In this work, we use the framework based on self-conditioned fields and hence, the terminology PDF instead of FDF.

The present work improves and extends the numerical implementation of LES/PDF methods. Specifically, we present a smoothing technique for spatial averaging of estimated statistics, an evaluation of three numerical implementations of the mixing model with molecular transport and a brief study of the effects of differential diffusion in a simple non-reacting mixing problem.

In a composition-PDF approach, although the effects of reaction appear in closed form and need no modeling, the effects of turbulent transport and molecular mixing need to be modeled. Typically, the effects of turbulent transport are modeled using a gradient diffusion hypothesis. To model the effects of molecular diffusion which appear as a conditional scalar dissipation term in the PDF transport equation, various mixing models have been developed. The Interaction by Exchange with the Mean (IEM) model was postulated in the context of chemical reactor engineering [14]. An identical model called the linear mean-square estimation model (LMSE) was proposed independently by [15]. These models are implemented as being local in physical space for inhomogeneous flows. The Interaction by Exchange with the Conditional Mean (IECM) mixing model [16,17] is designed to be local in velocity space while the Euclidean Minimum Spanning Tree (EMST) mixing model [18] models mixing as being local in composition space. Various other mixing models have been developed such as the MC (Modified Curl) mixing model [19–22] and MMC (Multiple Mapping Conditioning) mixing models [23,24]. In PDF methods, the choice of a mixing model is significant, for instance, to predict local extinction in Sandia flames E and F [25]. However, recent studies have shown that in LES/PDF methods, the subgrid-scale mixing closure provided by the IEM mixing model is adequate in most practical situations [26]. Therefore, in the current work, we employ the IEM mixing model to close the conditional dissipation term in the PDF transport equation.

The modeled PDF transport equation is solved using Lagrangian Monte Carlo particle methods. One of the initial works that established a formal relationship between particle models and PDF methods was by Pope [27]. The Lagrangian particle methods associated with the PDF transport in the form in use today are based on Pope's 1985 paper [7]. Here, the turbulent flow is represented by a large number of notional particles, all of which are considered to be statistically independent. Models are constructed to evolve the properties of the particles in time. The resulting stochastic differential equations (SDE) are solved to account for particle transport, mixing and reaction. Solving for the evolution of these particles corresponds to the solution of the modeled PDF transport equation. The first use of this approach to LES/PDF is due to Colucci et al. [11].

The conditional diffusion term in the PDF transport equation represents both molecular transport in physical space and molecular mixing in composition space. In most previous studies, the effects of molecular transport are incorporated as a random walk term in the particle transport equation, as first proposed by Anand and Pope [28]. Recently, McDermott and Pope [29] show that modeling the effects of molecular transport as a random walk in the particle position equation results in a spurious production of scalar variance in the DNS limit. They propose an alternative approach to modeling molecular transport as a mean drift term in the particle scalar evolution equation, and this avoids the spurious production of variance. LES studies of a laboratory-scale turbulent flame (Sandia flame D) [30] also show that on reasonably resolved grids, the molecular diffusivity is dominant as compared to the subgrid turbulent diffusivity in the near-field of the jet, indicating that the effects of molecular transport need to be treated accurately in LES/PDF models of turbulent reacting flows.

The current work is based on the models and algorithms implemented in the HPDF code described by Wang and Pope [31]. Micro-mixing is modeled using the IEM mixing model and the effects of molecular transport are modeled as a mean drift term as mentioned above [29]. This modeling strategy has the additional advantage of being able to account for the effects of differential diffusion. The mixing model is implemented such that problems of interest in both Cartesian and cylindrical coordinate systems can be effectively handled. We also require that the numerical schemes used to implement mixing satisfy the following criteria: (1) they satisfy detailed scalar conservation, (2) they ensure realizability, (3) they are stable and (4) they are accurate.

A typical PDF calculation of a turbulent reacting flow is performed with a nominal number, N_{pc}, of 20–50 particles per finite volume cell. In order to maintain an acceptable distribution of particles in space, various particle number control algorithms are used [9,32]. The numerical errors associated with a hybrid particle/mesh methodology can be classified broadly into statistical error, bias error, spatial truncation error and temporal discretization error. Among these, the statistical error is of random nature while the latter three are deterministic and cannot be reduced by averaging. The statistical error scales as

$N_{pc}^{-1/2}$ and the bias error scales as N_{pc}^{-1}; and both arise due to the finite number of particles used in the PDF calculations [33–35]. In previous studies, time averaging has been effectively used in PDF methods [33,34,36,37]. But in LES/PDF, since the fields are not stationary, time averaging cannot be used. In this study, we introduce smoothing, a form of spatial averaging.

In this work, we address the following issues. First, we evaluate for accuracy and computational cost, three numerical implementations of the IEM mixing model with molecular transport incorporated as a mean drift term. Secondly, we describe an implicit smoothing algorithm for variance reduction and assess its efficacy. Finally, we develop a methodology for accurately accounting for the effects of differential diffusion and test this implementation in a simple non-reacting mixing problem. The new implementations developed and evaluated here represent a significant advance in accuracy and computational efficiency over previous methods, and allow for the accurate representation of molecular diffusion, including differential diffusion.

2. Modeling of mixing and molecular transport

This section elaborates on the modeling of molecular transport and mixing in PDF studies and is divided into two parts. The first part under Section 2.1 briefly describes the set of SDEs used to evolve particle properties in time. Following this, Section 2.2 discusses the implied PDF transport equation and its moments.

2.1. Mixing model

Consider a PDF calculation of a turbulent non-reacting flow in which the fluid is represented by N_{tot} particles. We consider here a single composition, ϕ. The extension to multiple compositions ϕ_α with equal molecular diffusivities follows straightforwardly. The case of unequal diffusivities is considered in Section 6. The general particle has position $\mathbf{x}^*(t)$, mass $m^*(t)$ and a single composition $\phi^*(t)$. These particle properties are advanced in time by the following set of stochastic differential equations,

$$d\mathbf{x}^*(t) = \left[\widetilde{\mathbf{U}} + \frac{\nabla\bar{\rho}\Gamma_T}{\bar{\rho}}\right]^* dt + \sqrt{2\Gamma_T^*}\, d\mathbf{W}, \tag{1}$$

$$d\phi^*(t) = -\Omega_m^*(\phi^* - \tilde{\phi}^*)dt + \left[\frac{1}{\bar{\rho}}\frac{\partial}{\partial x_j}\left(\bar{\rho}\Gamma\frac{\partial\tilde{\phi}}{\partial x_j}\right)\right]^* dt + S^* dt, \tag{2}$$

where $\widetilde{\mathbf{U}}(\mathbf{x},t)$ is the resolved velocity, $\bar{\rho}(\mathbf{x},t)$ is the density, $\Gamma_T(\mathbf{x},t)$ is the turbulent subgrid-scale diffusivity, $\Gamma(\mathbf{x},t)$ is the molecular diffusivity, $\Omega_m(\mathbf{x},t)$ is the mixing frequency, $S(\mathbf{x},t)$ is the source term due to reaction, $\tilde{\phi}(\mathbf{x},t) = \langle\phi^*(t)|\mathbf{x}^*(t) = \mathbf{x}\rangle$ is the mean composition and $d\mathbf{W}$ is the incremental Wiener process. All quantities denoted with a superscript '$*$' are evaluated at $(\mathbf{x}^*(t),t)$ and particle properties are also denoted with a superscript '$*$'. Einstein's summation convention is followed except for repeated indices in parentheses. As is the notation used in standard LES, an over-line '$\bar{\ }$' denotes filtering operation and a tilde '$\tilde{\ }$' is used to denote density-weighted filtering. Or, following [13], $\tilde{\phi}$ can be viewed as a conditional mean, and $\tilde{\phi}$ the density-weighted conditional mean.

As first observed by McDermott and Pope [29], the mixing step corresponding to Eq. (2) has several advantages compared to the IEM mixing model. Firstly, it has the capability to include for the effects of differential diffusion directly into the mixing step: Eq. (2) can be written for different scalars, ϕ_α^*, each having its own molecular diffusivity Γ_α. Secondly, as will be re-emphasized in Section 2.2, this model which is a combination of the IEM mixing,

$$\frac{d\phi^*(t)}{dt} = -\Omega_m^*(\phi^* - \tilde{\phi}^*), \tag{3}$$

and a mean drift term corresponding to

$$\frac{\partial\tilde{\phi}}{\partial t} = \frac{1}{\bar{\rho}}\frac{\partial}{\partial x_j}\left(\bar{\rho}\Gamma\frac{\partial\tilde{\phi}}{\partial x_j}\right), \tag{4}$$

does not give rise to spurious production of scalar variance.

2.2. The implied PDF transport equation

The corresponding transport equation for the implied scalar PDF $f_\phi(\psi;\mathbf{x},t)$ (where ψ is the sample space variable for the scalar) can be derived from Eqs. (1) and (2) as

$$\frac{\partial f_\phi}{\partial t} + \frac{\partial}{\partial x_j}\left[f_\phi\left(\widetilde{U}_j + \frac{1}{\bar{\rho}}\frac{\partial\bar{\rho}\Gamma_T}{\partial x_j}\right)\right] = \frac{\partial^2(\Gamma_T f_\phi)}{\partial x_j\partial x_j} + \frac{\partial}{\partial\psi}\left[f_\phi\Omega_m\left(\psi - \tilde{\phi}\right)\right] - \frac{\partial}{\partial\psi}\left[f_\phi\frac{1}{\bar{\rho}}\frac{\partial}{\partial x_j}\left(\bar{\rho}\Gamma\frac{\partial\tilde{\phi}}{\partial x_j}\right)\right] + \frac{\partial}{\partial\psi}[f_\phi S]. \tag{5}$$

Given the transport equation for the PDF, the transport equation for the various implied moments can be obtained. Here, we mention the transport equations for the first two moments of the scalar to be:

$$\frac{\partial \bar{\rho}\tilde{\phi}}{\partial t}+\frac{\partial \bar{\rho}\widetilde{U}_j\tilde{\phi}}{\partial x_j}=\frac{\partial}{\partial x_j}\left[\bar{\rho}(\Gamma_T+\Gamma)\frac{\partial \tilde{\phi}}{\partial x_j}\right]+\bar{\rho}\widetilde{S}, \tag{6}$$

$$\frac{\partial \bar{\rho}\widetilde{\phi^2}}{\partial t}+\frac{\partial \bar{\rho}\widetilde{U}_j\widetilde{\phi^2}}{\partial x_j}=\frac{\partial}{\partial x_j}\left[\bar{\rho}\Gamma_T\frac{\partial \widetilde{\phi^2}}{\partial x_j}\right]+2\tilde{\phi}\frac{\partial}{\partial x_j}\left[\bar{\rho}\Gamma\frac{\partial \tilde{\phi}}{\partial x_j}\right]-2\bar{\rho}\Omega_m(\widetilde{\phi^2}-\tilde{\phi}^2)+2\bar{\rho}\widetilde{S\phi}. \tag{7}$$

From Eqs. (6) and (7), the transport equation for the subgrid variance of the scalar, $Z=\widetilde{\phi^2}-\tilde{\phi}^2$ can be obtained as,

$$\frac{\partial \bar{\rho}Z}{\partial t}+\frac{\partial \bar{\rho}\widetilde{U}_jZ}{\partial x_j}=\frac{\partial}{\partial x_j}\left[\bar{\rho}\Gamma_T\frac{\partial Z}{\partial x_j}\right]-2\bar{\rho}\Omega_mZ+2\bar{\rho}\Gamma_T\frac{\partial \tilde{\phi}}{\partial x_j}\frac{\partial \tilde{\phi}}{\partial x_j}+2\bar{\rho}(\widetilde{S\phi}-\widetilde{S}\tilde{\phi}). \tag{8}$$

Eq. (8) contains a production term due to turbulent subgrid diffusivity but no production term due to molecular diffusivity. In the DNS limit, the production due to turbulent diffusivity vanishes and there is no production of scalar variance, contrary to a model that includes for the effects of molecular diffusivity as a random walk term in the particle position equation [29].

In summary, it is to be noted that the particle model comprising of Eqs. (1) and (2) avoids spurious variance production and has the potential to account for differential diffusion effects.

3. Numerical implementation of mixing and molecular transport

The numerical method employed here is the hybrid particle/mesh method [4]. A structured mesh is used to store mean quantities estimated from particle data at the cell center locations, which are then interpolated onto particle locations.

To illustrate some of the issues involved, we describe now a crude numerical implementation of the particle mesh method for a simplified problem. We consider constant-density flow in a one-dimensional periodic domain of length L with x^* being distributed uniformly. Eqs. (1) and (2) reduce to,

$$dx^*(t)=\left[\widetilde{U}+\frac{\partial \Gamma_T}{\partial x}\right]^*dt+\sqrt{2\Gamma_T^*}dW, \tag{9}$$

$$\frac{d\phi^*(t)}{dt}=-\Omega_m^*(\phi^*-\tilde{\phi}^*)+\frac{\partial}{\partial x}\left(\Gamma\frac{\partial \tilde{\phi}}{\partial x}\right)^*. \tag{10}$$

As sketched in Fig. D.1, the domain is partitioned into N_{cell} cells of width $\Delta x=L/N_{\text{cell}}$. Given the particle properties at time t, and given a small time-step Δt, the crude numerical implementation obtains the particle properties at time $t+\Delta t$ through a sequence of processes now described. It is emphasized that this implementation has many deficiencies and is described solely to introduce some of the issues faced in any implementation.

1. Given the values of $\widetilde{U}$, Γ_T and $\partial\Gamma_T/\partial x$ at cell centers, an interpolation scheme is used to obtain the values of the coefficients in Eq. (9) at the particle locations. As sketched in Fig. D.2, possible interpolation schemes include: piece-wise constant (PC); piece-wise linear (PL); and linear spline (LS).
2. The particle positions are advanced by

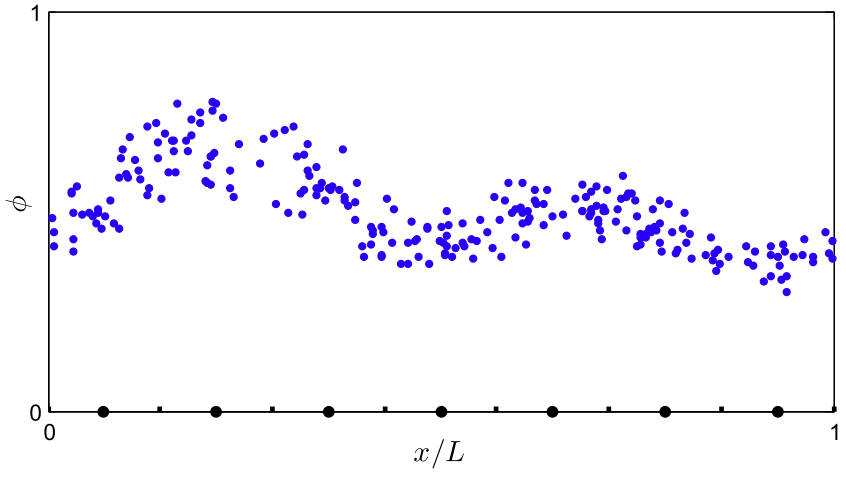

Fig. D.1. Sketch of the periodic domain of length L: showing the particles properties (x^*,ϕ^*); the $N_{\text{cell}}=7$ cells; and the cell centers (circles) on the abscissa.

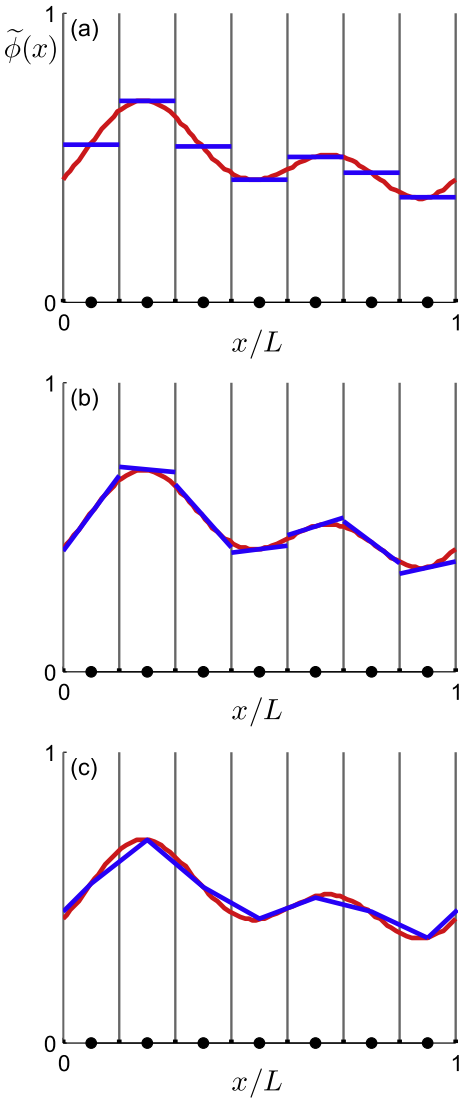

Fig. D.2. Illustration of different interpolation schemes (blue) used to approximate the field $\tilde{\phi}(x)$ (red): (a) piece-wise constant (PC), (b) piece-wise linear (PL) and (c) linear spline (LS). (For interpretation of the references to color in this figure legend, the reader is referred to the web version of this article.)

$$x^*(t+\Delta t) = x^*(t) + \left[\widetilde{U} + \frac{\partial \Gamma_T}{\partial x}\right]^* \Delta t + \left(2\Gamma_T^* \Delta t\right)^{\frac{1}{2}} \eta^*, \tag{11}$$

where η^* is a standardized Gaussian random variable independent for each particle and for each time step.

3. Given the particle compositions $\phi^*(t)$, an estimate $\hat{\phi}_j$ is made of the mean composition at the jth cell center. The simplest estimate – termed "particle-in-cell" (PIC) – is the ensemble mean of all particles in the jth cell. An alternative – termed "cloud-in-cell" (CIC) – is to form the ensemble mean of all particles, weighted by the linear basis function centered at the jth cell center. Both methods can be viewed as kernel estimators, with the different kernels $K_j(x)$ sketched in Fig. D.3.
4. To reduce the statistical error in the estimated means at cell centers $\hat{\phi}_j$, smoothing can be performed, to yield modified estimators $\tilde{\phi}_j$. This can most simply be achieved by the explicit three-point smoothing

$$\tilde{\phi}_j = (1-2\beta_s)\hat{\phi}_j + \beta_s(\hat{\phi}_{j-1} + \hat{\phi}_{j+1}) \tag{12}$$

for specified positive β_s (stability requires $\beta_s \leqslant 0.5$). We can also consider implicit smoothing, the simplest three-point scheme being

$$(1+2\alpha_s)\tilde{\phi}_j - \alpha_s(\tilde{\phi}_{j-1} + \tilde{\phi}_{j+1}) = \hat{\phi}_j \tag{13}$$

for specified positive α_s.

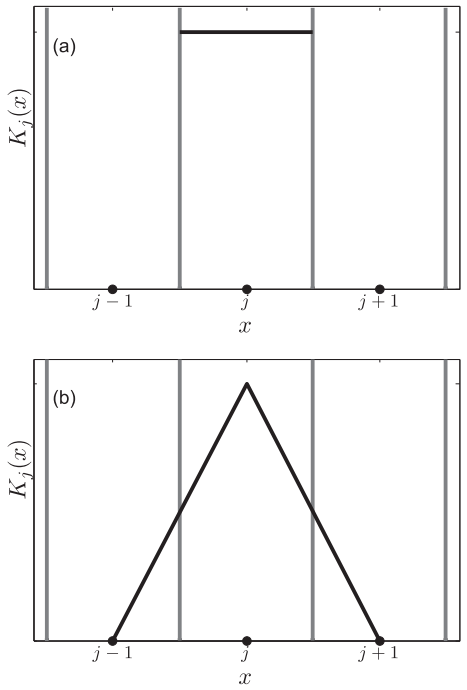

Fig. D.3. Kernels $K_j(x)$ used to estimate means at the center of cell j: (a) PIC and (b) CIC.

5. Based on the last term in Eq. (10), the unsteady heat conduction equation

$$\frac{\partial\tilde{\phi}}{\partial t}=\frac{\partial}{\partial x}\left(\Gamma\frac{\partial\tilde{\phi}}{\partial x}\right) \tag{14}$$

is integrated for a time Δt by a finite-difference method, starting from the smoothed cell-centered values $\tilde{\phi}$. The change in the solution over the time-step is referred to as the "mean drift" and its value at the jth cell center is denoted by $\Delta\tilde{\phi}_j$.
6. The values of $\Omega_m, \tilde{\phi}$ and $\Delta\tilde{\phi}$ are interpolated onto the particles, and then Eq. (10) is advanced in time by

$$\phi^*(t+\Delta t)=\phi^*(t)+\Delta\tilde{\phi}^*-\Omega_m^*\Delta t(\phi^*(t)-\tilde{\phi}^*). \tag{15}$$

Having introduced this rudimentary particle-mesh scheme for the simplified one-dimensional problem, we now consider the criteria by which this and other implementations can be appraised.

1. Stability: obviously, unconditional stability is desirable. The above scheme is likely to be unstable if β_s and $\Omega_m\Delta t$ are too large.
2. Accuracy: the numerical errors introduced in this type of particle-mesh scheme include
   (a) A temporal splitting error due to considering simultaneous processes sequentially. The crude splitting scheme above dooms the overall method to first-order temporal accuracy.
   (b) Temporal truncation errors in the sub-steps *e.g.*, Eqs. (11), (14) and (15).
   (c) Spatial truncation errors involved in interpolation and in advancing the heat conduction equation.
   (d) Spatial smearing errors due to the smoothing operation, and the estimation of means.
   (e) Statistical errors due to having a finite total number of particles N_{tot}. For example, the statistical error in the estimated mean $\hat{\phi}_j$ varies as $N_{\text{pc}}^{-1/2}$, where $N_{\text{pc}}\equiv N_{\text{tot}}/\text{N}_{\text{cell}}$ is the average number of particles per cell.
   (f) Bias errors, which are deterministic errors due to N_{tot} being finite.
   Thus, a suitably defined root-mean-squared error in the scheme $\mathcal{E}$ can be modeled as

$$\mathcal{E}=a\Delta x^p+b\Delta t^q+cl_s^r+\frac{d}{N_{\text{eff}}}+\frac{e}{\sqrt{N_{\text{eff}}}}, \tag{16}$$

   where a, b, c, d and e are constants and the terms on the right-hand side represent, respectively: spatial truncation error; temporal errors; smearing error, where l_s is the smearing length-scale associated with the smoothing (determined by α_s and β_s); bias, where N_{eff} is an effective number of particles used to estimate means; and statistical error. If no smoothing is used, then N_{eff} equals N_{pc}; with smoothing, N_{eff} increases with l_s. The scheme described above is

most likely first-order accurate in space and time ($p = 1, q = 1, r = 1$), whereas the method described below is second-order accurate ($p = 2, q = 2, r = 2$).

3. Computational cost: this is normally dominated by the work that scales linearly with the number of particles, N_{tot}, the work which scales with the number of cells being small in comparison.
4. Conservation: it follows from Eq. (10) that the sum of $\phi^*(t)$ over all particles is conserved. It is desirable that a numerical implementation have this same conservation property. The scheme above is not conservative.
5. Boundedness: composition variables such as mixture fraction and species mass fractions are bounded; in particular, they are non-negative. Subject to Ω_m being greater than a known lower limit, Eq. (10) satisfies boundedness which can be stated as,

$$\min\{\phi^*(t)\} \leqslant \phi^*(t + \Delta t) \leqslant \max\{\phi^*(t)\}. \tag{17}$$

6. Continuity: the mean composition $\tilde{\phi}(x, t)$ implied by Eqs. (9) and (10) is smooth (as is the PDF of ϕ^*), provided that the coefficients vary smoothly. Discontinuous interpolation schemes (PC and PL) introduce discontinuities in the solution, which may be undesirable.

The most accurate scheme presented below (denoted CIC-LS with smoothing) has the following attributes: it is unconditionally stable, second-order accurate in space and time, the statistical error scales as $N_{\text{tot}}^{-1/2}$ (as opposed to $N_{\text{pc}}^{-1/2}$), it satisfies conservation and boundedness, and yields continuous solutions.

The following sub-sections describe the details of the numerical method used in this work and are organized as follows. The first part Section 3.1 elaborates on the splitting scheme adopted. The primary focus of this section is on the implementation of mixing and molecular transport. Section 3.2 details two mean estimation methods while Section 3.3 presents three interpolation schemes and finally, the fourth section focuses on the details of the smoothing algorithm.

3.1. Splitting scheme

Given the stochastic differential equations used to advance particle properties in time [Eqs. (1) and (2)], the following splitting scheme is used to solve for particle transport $\mathbb{T}$, reaction $\mathbb{R}$ and mixing $\mathbb{M}$. The mixing step here refers to the combination of IEM mixing and the mean drift due to molecular transport. The splitting scheme [38] considered here is of the type, $\mathbb{TMRMT}$, where each of the transport and mixing sub-steps are performed twice each for half the time step, Δt, and the reaction step is performed once for one complete time step. The coefficients in the SDEs can be frozen at the mid-point while preserving the second-order accuracy, and the type of splitting $\mathbb{TMRMT}$ is proven to be second-order accurate [38].

The mixing step $\mathbb{M}$ consists of two sub-steps – IEM mixing $\mathbb{I}$ and estimation of mean drifts due to molecular diffusivity $\mathbb{D}$. Following [29], the mixing step $\mathbb{M}$ is solved using the splitting scheme, $\mathbb{IDI}$. The various quantities required to perform one step of mixing, such as Ω_m and Γ, are evaluated at the particle locations at the mid-point of the time step. This yields a one-step update for the particle scalar ϕ discussed below.

Consider advancing the scalar ϕ^* carried by the particle over a time step of Δt from time $t_n = n\Delta t$ to $t_{n+1} = (n + 1)\Delta t$. As mentioned earlier, the mixing frequency Ω_m and molecular diffusivity Γ are known at the time level $t_{n+\frac{1}{2}} = (n + \frac{1}{2})\Delta t$. Given that the scalar mean $\tilde{\phi}^n$ and the mean drift, $\Delta\tilde{\phi}^{n+\frac{1}{2}} = \tilde{\phi}^{n+1} - \tilde{\phi}^n$ are known at particle locations, the one-step update [29] for the particle scalar can be written as,

$$\phi^{*,n+1} = \phi^{*,n} + c^{*,n+\frac{1}{2}}(\tilde{\phi}^{*,n} - \phi^{*,n}) + \Delta\tilde{\phi}^{*,n+\frac{1}{2}}, \tag{18}$$

where

$$c^{n+\frac{1}{2}} = 1 - \exp\left(-\Omega_m^{n+\frac{1}{2}}\Delta t\right). \tag{19}$$

With details provided in subsequent subsections, the specific steps involved in implementing Eq. (18) to advance the particle scalar over a time step, $\Delta t = t_{n+1} - t_n$ are:

1. The mixing frequency $\Omega_m^{n+\frac{1}{2}}$ available at the cell centers of the PDF mesh is used to calculate $c^{n+\frac{1}{2}}$ at cell centers using Eq. (19)
2. The quantity $c^{n+\frac{1}{2}}$ is interpolated onto particle locations to obtain $c^{*,n+\frac{1}{2}}$ using any one of the interpolation methods given by Eqs. (25), (26) or (28).
3. Particle weights w^* defined by

$$w^* = m^* c^* \tag{20}$$

are evaluated.

4. Given particle scalar $\phi^{*,n}$ at time level n and the weights w^*, the scalar means $\hat{\phi}^n$ are estimated at the cell centers (Eq. (23)) along with the cell weights w using Eq. (24) defined below.
5. The estimates $\hat{\phi}^n$ of the scalar means are smoothed with weights w to obtain smoothed estimates of the means $\tilde{\phi}^n$ as given by Eq. (32) with $f = \hat{\phi}^n$ and $g = \tilde{\phi}^n$ with the specification given by Eq. (45)–(48).

6. The mean drifts $\Delta\tilde{\phi}^{n+\frac{1}{2}}$ are calculated from $\tilde{\phi}^n$ using Eq. (A.15) elaborated in Appendix A.1.
7. The boundedness condition is imposed on $c^{*,n+\frac{1}{2}}$ using Eq. (C.4).
8. Steps 3–5 are repeated with the modified values of $c^{*,n+\frac{1}{2}}$.
9. The mean drifts $\Delta\tilde{\phi}^{n+\frac{1}{2}}$ and the smoothed means $\tilde{\phi}^n$ are interpolated onto particle locations to obtain $\Delta\tilde{\phi}^{*,n+\frac{1}{2}}$ and $\tilde{\phi}^{*,n}$, respectively, from Eq. (25), (26) or (28).
10. Finally, the one-step particle scalar update, Eq. (18), is performed.

For the most part, we consider the case of uniform particle masses, particularly in the analysis of the scheme. In practice, non-uniform particle masses are used, and there is no difficulty in applying the method in such cases. The algorithm indicates that the following operations need to be performed: (1) estimation of means given particle properties, (2) estimation of mean drifts, (3) interpolation of mean quantities to particle locations and (4) smoothing. The following subsection describes the two numerical schemes used for mean estimation.

3.2. Estimation of means

In this section, we present the details of two numerical schemes used to estimate the means from particle properties *viz.*, particle-in-cell (PIC) and cloud-in-cell (CIC) based on a uniform Cartesian grid, equal in each direction. However, the methods are not restricted to this specific case. Consider $\mathbf{x}_j$ to denote the cell center locations of the PDF mesh with cell volume Δx^3. Let $\mathbf{e} = (\mathbf{e}_1, \mathbf{e}_2, \mathbf{e}_3)$ denote the unit vectors in the three coordinate directions.

Let us define the indicator function for the cell centered at $\mathbf{x}_j$, denoted $\mathbf{I}_j(\mathbf{y})$ as $\mathbf{I}_j(\mathbf{y}) = \prod_{k=1}^{3} I_{j,k}(\mathbf{y})$ where,

$$I_{j,k}(\mathbf{y}) = \begin{cases} 1, & \text{for } |(\mathbf{y}-\mathbf{x}_j)\cdot\mathbf{e}_k| < \Delta x/2, \\ 0, & \text{otherwise.} \end{cases} \tag{21}$$

Similarly, consider linear B-spline basis functions $\mathbf{B}_j(\mathbf{y})$ for the cell centered at $\mathbf{x}_j$ to be defined as $\mathbf{B}_j(\mathbf{y}) = \prod_{k=1}^{3} B_{j,k}(\mathbf{y})$ with

$$B_{j,k}(\mathbf{y}) = \begin{cases} 1 - \frac{|(\mathbf{y}-\mathbf{x}_j)\cdot\mathbf{e}_k|}{\Delta x/2}, & \text{for } |(\mathbf{y}-\mathbf{x}_j)\cdot\mathbf{e}_k| < \Delta x/2 \\ 0, & \text{otherwise.} \end{cases} \tag{22}$$

For particle weights w^* given by Eq. (20), the mean $\hat{\phi}_j$, at a cell centered at $\mathbf{x}_j$ is estimated from particles as,

$$\hat{\phi}_{(j)} w_{(j)} = \sum_p \mathbf{K}_j(\mathbf{x}_p^*) w_p^* \phi_p^*, \tag{23}$$

where w_j, the weight associated with that cell is estimated as,

$$w_j = \sum_p \mathbf{K}_j(\mathbf{x}_p^*) w_p^* \tag{24}$$

for some kernel-estimation method with kernel $\mathbf{K}_j$ and the index p runs over all the particles in the PDF domain. We show later in Appendix C.2 that w^* defined by Eq. (20) satisfies detailed conservation. The PIC scheme is obtained for $\mathbf{K}_j = \mathbf{I}_j$ and likewise, $\mathbf{K}_j = \mathbf{B}_j$ gives rise to the CIC scheme [29].

3.3. Interpolation onto particles

In this subsection, the three schemes – piecewise-constant (PC), piecewise-linear (PL) and linear splines (LS) – used to interpolate mean quantities onto particle locations are detailed. Piecewise-constant interpolation is the simplest but is only first-order accurate. Piecewise-linear interpolation is second-order accurate and an improvement on piecewise-constant interpolation. Neither piecewise-constant interpolation nor piecewise-linear interpolation results in continuous fields. Interpolation using linear splines satisfies both second-order accuracy and continuity. The details of each of the interpolation schemes are now presented:

Piecewise-constant (PC) interpolation of $\tilde{\phi}$ onto a particle located at $\mathbf{x}_p^*$ is performed as,

$$\tilde{\phi}_p^* = \sum_j \mathbf{I}_j\left(\mathbf{x}_p^*\right)\tilde{\phi}_j, \tag{25}$$

while interpolation using linear spline basis functions (LS) is achieved by,

$$\tilde{\phi}_p^* = \sum_j \mathbf{B}_j\left(\mathbf{x}_p^*\right)\tilde{\phi}_j. \tag{26}$$

The PC and the LS schemes can be jointly represented using $\mathbf{K}_j$ defined in Section 3.2 as,

$$\tilde{\phi}_p^* = \sum_j \mathbf{K}_j\left(\mathbf{x}_p^*\right)\tilde{\phi}_j. \tag{27}$$

The third interpolation scheme – the piecewise linear (PL) interpolation – is formulated as,

$$\tilde{\phi}_p^* = \sum_j \mathbf{I}_j\left(\mathbf{x}_p^*\right)\tilde{\phi}_j + \zeta \sum_j \mathbf{I}_j\left(\mathbf{x}_p^*\right)\left(\mathbf{x}_p^* - \bar{\mathbf{x}}_j\right)\cdot \boldsymbol{v}_j, \tag{28}$$

where $\bar{\mathbf{x}}_j$ is given by,

$$\bar{\mathbf{x}}_j = \frac{\sum_p \mathbf{I}_j\left(\mathbf{x}_p^*\right) w_p^* \mathbf{x}_p^*}{\sum_p \mathbf{I}_j\left(\mathbf{x}_p^*\right) w_p^*} \tag{29}$$

and $\boldsymbol{v}_j$ (an approximation to $\nabla\tilde{\phi}_j$ when the interpolant is $\tilde{\phi}$) is given by,

$$\boldsymbol{v}_j = \mathbf{e}_k \delta_k \tilde{\phi}_j. \tag{30}$$

In Eq. (30), δ_k denotes the central-differencing operator in the kth direction. In Eq. (28), the parameter ζ is taken to be the maximum value of $\tilde{\zeta} \in [0,1]$ such that $\tilde{\phi}^*$ satisfies the boundedness condition given by Eq. (17). To compare the three interpolation schemes, it is to be noted that while both PC and LS interpolation schemes naturally satisfy boundedness criterion, PL requires ζ to explicitly impose the boundedness condition.

Thus, there are two mean estimation methods and three interpolation schemes. Due to the conservation criterion given by Eq. (C.1), only three combinations are considered in this work. The following combinations of schemes satisfy detailed conservation: PIC-PC, PIC-PL and CIC-LS as shown in Appendix C. The properties of each of these schemes are summarized in Table D.1. All calculations shown in Section 5.1 are aimed at evaluating these three numerical implementations of mixing and molecular transport for efficiency and accuracy. Next, we present the details of the implicit smoothing scheme developed.

3.4. Smoothing

Several 'variance reduction' techniques have been described in previous studies [33,34,36,37]. But these variance reduction techniques are presented as time-averaging methods that are suitable to be used with statistically-stationary flows. In LES/PDF methods, the fields are not statistically stationary and therefore, time-averaging cannot be used. Here, we present a smoothing algorithm based on spatial averaging. There are two types of quantities of interest to us that need smoothing – quantities used for output, referred to as "output quantities" and those that are fed back into the calculation, referred to as "feedback quantities". Of specific interest in this work are quantities fed back into the mixing model, such as the scalar means.

A variance reduction method, intended to be used in conjunction with the numerical implementation of a mixing model, should be formulated such that the operation is conservative, ensures boundedness and preserves regularity of the input fields. Moreover, the smearing error incurred (due to spatial averaging) should be small. In this section, we elaborate on an implicit smoothing methodology derived based on the heat diffusion equation. First, Section 3.4.1 introduces this smoothing scheme. Following this, Section 3.4.2 lists the properties of the smoothing scheme. Finally, Sections 3.4.3 and 3.4.4 elaborate on the specification of the smoothing operator and its interpretation.

3.4.1. A brief introduction

Consider, in one-dimensional space, a periodic domain of size L. Consider a discrete set of points given by $\mathbf{x}_j$ with uniform spacing Δx. We are given a noisy input function, $f_j = f(\mathbf{x}_j)$, at each of these points and we want to form a smoothed version of it, $g_j = g(\mathbf{x}_j)$, such that the variance of g is less than the variance of f. Such a smoothing scheme can be obtained as a solution to the heat conduction equation. It is to be noted that the smoothing operation can be performed either explicitly or implicitly or a combination thereof, as shown in Appendix B.1, but here we focus on the implicit smoothing methodology. Therefore, at each $\mathbf{x}_j$, g_j is defined as

$$(W_{ij} + A_{ij})g_j = W_{ij} f_j, \tag{31}$$

which we re-write in an obvious matrix notation as

$$(W + A)g = Wf, \tag{32}$$

Table D.1
Comparison of the various numerical schemes against the set of criteria listed in Section 3. The symbols indicate: Y – naturally satisfied; I – imposed; N – not satisfied.

Property	PIC-PC	PIC-PL	CIC-LS
Conservation	Y	I	Y
Boundedness	Y	I	Y
Continuity	N	N	Y
Unconditional stability	Y	Y	Y
Second-order accuracy	N	Y	Y

where $W = \mathrm{diag}(w_i)$ represents the weights ascribed to each of the grid points, $\mathbf{x}_j$ and the matrix A is the implicit smoothing matrix, parametrized by the smoothing parameter α_s. The particulars regarding the specification of each of the matrices are detailed in Section 3.4.3. Note that Eq. (13) is a particular form of Eq. (32), in which the weights are unity, and A is symmetric, tri-diagonal, with components $[\,-\alpha_s \quad 2\alpha_s \quad -\alpha_s\,]$.

For multi-dimensional problems, the smoothing algorithm is implemented using the Locally One Dimensional (LOD) variant of the Alternating Direction Implicit (ADI) scheme (Appendix A) appropriately adapted to the smoothing methodology. In the LOD scheme, the smoothing algorithm is applied in each direction successively thus approximating the solution to a multi-dimensional problem by a collection of successive solutions to an equivalent system of one-dimensional problems. Therefore, the subsequent sections describe the details of the smoothing methodology in one dimension.

3.4.2. Properties

We require the following properties of the smoothing matrix, A, and the weight matrix, W:

$$A_{ij} \leqslant 0, \quad i \neq j, \tag{33}$$

$$\sum_i A_{ij} = 0, \tag{34}$$

$$A_{ij} = A_{ji}, \tag{35}$$

$$\det(W + A) \neq 0, \tag{36}$$

$$W_{ij} = 0, \quad i \neq j, \tag{37}$$

$$W_{ii} \geqslant 0. \tag{38}$$

We then deduce the following properties of g:

- Conservation: Conservation requires that the weighted sum of the input field f equals the weighted sum of the smoothed field g. Consider summing over all rows of Eq. (31) as,

$$\sum_i w_i g_i + \sum_j \sum_i A_{ij} g_j = \sum_i w_i f_i. \tag{39}$$

  Using the property that the elements of a given column of A sum to zero, given by Eq. (34), reduces the second term in Eq. (39) to zero and therefore,

$$\sum_i w_i g_i = \sum_i w_i f_i \tag{40}$$

  showing that smoothing satisfies the conservation criterion.
- Boundedness: The operation of smoothing should preserve the boundedness of the input quantities. Let us again consider Eq. (31) to be re-expressed as,

$$(w_i + A_{ii}) g_i = w_i f_i - \sum_{j \neq i} A_{ij} g_j, \tag{41}$$

$$g_i = \mu_i f_i + \sum_{j \neq i} \mu_j g_j, \tag{42}$$

  where

$$\mu_i = \frac{w_i}{w_i + A_{ii}}, \tag{43}$$

$$\mu_j = -\frac{A_{ij}}{w_i + A_{ii}}, \quad i \neq j. \tag{44}$$

  It follows that μ is a partition of unity *i.e.* $\mu_j \geqslant 0,\ \sum_j \mu_j = 1$. Then Eq. (42) shows that g_i is a convex combination of f_i and g_j for $i \neq j$ and it follows that g_i cannot be an isolated vertex of the convex hull $\mathrm{conv}(f, g)$ and hence g_i is in $\mathrm{conv}(f)$. Thus g_i satisfies the boundedness condition.

3.4.3. Details of the smoothing scheme

Various families of smoothing schemes are briefly mentioned in Appendix B.1 but the three-point implicit smoothing scheme is considered in this work and is the focus of the current section. Consider a three-point implicit smoothing scheme parametrized by α_s with the following definitions for A and W:

$$A_{jj-1} = -\alpha_s \frac{w_{j-1} + w_j}{2}, \tag{45}$$

$$A_{jj+1} = -\alpha_s \frac{w_{j+1} + w_j}{2}, \tag{46}$$

$$A_{jj} = -(A_{jj-1} + A_{jj+1}), \tag{47}$$

$$W_{jj} = w_j. \tag{48}$$

This specification for A and W is conservative and ensures boundedness. The implication of α_s becomes evident upon considering the length scales associated with the smoothing operation and is elaborated in the following section.

3.4.4. Length scales in smoothing

The process of smoothing results in the spatial smearing of the input fields as it achieves a non-trivial reduction in its variance. We define two relevant length scales: l_s associated with smearing; and l_v associated with variance reduction. We perform the analysis for smoothing with unity weights in one-dimension for simplicity but the analysis is not restricted to this specific case.

Consider a three-point implicit smoothing scheme with unity weights in one-dimension such that Eq. (32) reduces to

$$(I + A)g = f. \tag{49}$$

Further, we define an equivalent explicit smoothing operator $C \equiv (I + A)^{-1}$ and represent Eq. (49) as

$$g = Cf, \tag{50}$$

whose Fourier transform is given by Eq. (B.12). Given the Fourier transform $\widehat{C}(\kappa; \Delta x)$ of C in Eq. (B.13) in terms of the wavenumber κ and grid spacing Δx, we deduce the following properties of C:

- The zeroth moment M_0 is unity or equivalently,

$$M_0 = \widehat{C}(0; \Delta x) = 1. \tag{51}$$

- The second moment evaluates to

$$M_2 = -\left(\frac{\partial^2 \widehat{C}}{\partial \kappa^2}\right)_{\kappa=0} = 2\alpha_s \Delta x^2. \tag{52}$$

- All the odd moments are zero,

$$M_{2n+1} = \left(\frac{\partial^{2n+1} \widehat{C}}{\partial \kappa^{2n+1}}\right)_{\kappa=0} = 0, \quad \text{for } n \geqslant 0. \tag{53}$$

We then define l_s such that the second moment, M_2 is obtained as,

$$M_2 \equiv \frac{1}{8} l_s^2. \tag{54}$$

The reason for the proportionality constant of 8 in Eq. (54) becomes clear below. Comparing Eq. (54) with Eq. (52) we obtain l_s to be,

$$\frac{l_s}{\Delta x} = \gamma \equiv 4\sqrt{\alpha_s}. \tag{55}$$

Next, the length scale l_v associated with variance reduction V is defined such that the variance reduction:

$$V \equiv \frac{\mathrm{var}(f)}{\mathrm{var}(g)}, \tag{56}$$

due to smoothing in a D-dimensional space is obtained as,

$$V \equiv \left(1 + \frac{l_v}{\Delta x}\right)^D. \tag{57}$$

The variance reduction is described exactly in Appendix B.3. Therefore, by equating Eq. (57) with Eq. (B.27), l_v can be obtained as,

$$\frac{l_v}{\Delta x} = \frac{(1 + 4\alpha_s)^{3/2}}{1 + 2\alpha_s} - 1 \tag{58}$$

for a three-point implicit smoothing operation. With this definition, $l_v/\Delta x$ tends to zero as $l_s/\Delta x$ tends to zero.

An approximation to $l_v/\Delta x$ is,

$$\frac{l_v}{\Delta x} \approx \frac{l_{va}}{\Delta x} \equiv \frac{\gamma^2}{\sqrt{16+\gamma^2}}. \tag{59}$$

This approximation is accurate to within 10%, and yields the correct limits for small and large γ. It is to be noted that for large γ, we have $l_v/\Delta x \sim \gamma = l_s/\Delta x$.

Moreover, for the case $f = \hat{\phi}$, where $\hat{\phi}$ is the unsmoothed estimate of the scalar mean based on N_{pc} particles, $\text{var}(f) \sim N_{\text{pc}}^{-1}$. We then define N_{eff} such that,

$$V = \frac{N_{\text{eff}}}{N_{\text{pc}}}. \tag{60}$$

As a result, Eqs. (57) and (60) yield,

$$N_{\text{eff}} = N_{\text{pc}}\left(1 + \frac{l_v}{\Delta x}\right)^D, \tag{61}$$

$$\approx N_{\text{pc}}\left(1 + \frac{\gamma^2}{\sqrt{16+\gamma^2}}\right)^D. \tag{62}$$

As presented in Section 5, we are interested in modeling the error (suitably defined) calculated based on the estimates of mean quantities. Since, the error analysis is more conveniently done with non-dimensional parameters, we define $l = l_s/L,\ h = \Delta x/L$ and $\tau = \Delta t/T$ where T is the total time for which a calculation is performed. Consequently, the effective number of particles, N_{eff} is obtained from Eq. (62) as,

$$N_{\text{eff}} = N_{\text{tot}}\left(h + \frac{l^2}{\sqrt{16h^2+l^2}}\right)^D. \tag{63}$$

In summary, a three-point implicit smoothing scheme is presented which satisfies conservation and boundedness criteria. Additionally, as is shown in Appendix B.1, the scheme is also successful in handling empty cells properly, and thereby preserves the regularity of input fields. The choice of α_s follows directly from the choice of the normalized smoothing length scale, l. Large values of l (as compared to h) result in large reductions in the variance. But, a large reduction in the variance is always accompanied by a large smearing error indicating the existence of an optimal choice of l (or, equivalently, for α_s).

4. The method of manufactured solutions

The Method of Manufactured Solutions (MMS) [39,40] is extensively used in the current work to appraise the different numerical schemes presented in Section 3 and this section provides a brief description of the methodology. MMS was originally used to verify the numerical solutions of partial differential equations by manufacturing analytical solutions to the set of equations being solved [41,42]. In [38], this method is extended for use in the verification of Monte Carlo particle methods. We follow an identical procedure in this work.

In order to advance particle properties in time using Eqs. (1) and (2), the coefficients $\bar{\rho},\ \widetilde{U},\ \Gamma,\ \Gamma_T,\ \Omega_m$ are required. In the MMS, these quantities are specified as functions of $\mathbf{x}$ and t. Additionally, constants R_o and J_o are specified to facilitate a simple closure for reaction, $S(\phi)$, using a linear model [38]:

$$S(\phi) = R_o(\phi - J_o). \tag{64}$$

In addition, the manufactured mean $\bar{\phi}_m$ and variance $\overline{\phi'^2}_m$ fields are also specified. Then additional source terms $S_m(\mathbf{x},t)$ and $S_v(\mathbf{x},t)$ are defined such that $\bar{\phi}_m$ and $\phi'^2{}_m$ satisfy the following equations:

$$\frac{\partial \bar{\rho}\bar{\phi}_m}{\partial t} + \frac{\partial \bar{\rho}\widetilde{U}_j\bar{\phi}_m}{\partial x_j} = \frac{\partial}{\partial x_j}\left[\bar{\rho}(\Gamma_T + \Gamma)\frac{\partial \bar{\phi}_m}{\partial x_j}\right] + \bar{\rho}R_o(\bar{\phi}_m - J_o) + \bar{\rho}S_m, \tag{65}$$

$$\frac{\partial \bar{\rho}\overline{\phi'^2}_m}{\partial t} + \frac{\partial \bar{\rho}\widetilde{U}_j\overline{\phi'^2}_m}{\partial x_j} = \frac{\partial}{\partial x_j}\left[\bar{\rho}\Gamma_T\frac{\partial \overline{\phi'^2}_m}{\partial x_j}\right] - 2\bar{\rho}\Omega_m\overline{\phi'^2}_m + 2\bar{\rho}\Gamma_T\frac{\partial \bar{\phi}_m}{\partial x_j}\frac{\partial \bar{\phi}_m}{\partial x_j} + 2\bar{\rho}R_o\overline{\phi'^2}_m + \bar{\rho}S_v. \tag{66}$$

These equations correspond to Eqs. (6) and (7) but with the addition of the source terms. The second moment is then obtained as,

$$\overline{\phi^2}_m = \bar{\phi}_m^2 + \overline{\phi'^2}_m. \tag{67}$$

The transport equation for the corresponding PDF, $g_\phi(\psi;\mathbf{x},t)$ is obtained as,

$$\frac{\partial g_\phi}{\partial t}+\frac{\partial}{\partial x_j}\left[g_\phi\left(\widetilde{U}_j+\frac{1}{\bar{\rho}}\frac{\partial \bar{\rho}\Gamma_T}{\partial x_j}\right)\right]=\frac{\partial^2(\Gamma_T g_\phi)}{\partial x_j\partial x_j}+\frac{\partial}{\partial\psi}[g_\phi\Omega_m(\psi-\tilde{\phi})]-\frac{1}{\bar{\rho}}\frac{\partial}{\partial x_j}\left[\bar{\rho}\Gamma\frac{\partial\tilde{\phi}}{\partial x_j}\right]\frac{\partial g_\phi}{\partial\psi}+\frac{\partial}{\partial\psi}(g_\phi S)-S_m\frac{\partial g_\phi}{\partial\psi}+\frac{\partial}{\partial\psi}[g_\phi\Omega_v(\psi-\tilde{\phi})], \tag{68}$$

where $\Omega_v=-S_v/2\overline{\phi'^2}_m$ and the implied particle model for scalar evolution can be derived to be,

$$d\phi^*(t)=-\Omega_m^*\left(\phi^*-\tilde{\phi}^*\right)dt+\left[\frac{1}{\bar{\rho}}\frac{\partial}{\partial x_j}\left(\bar{\rho}\Gamma\frac{\partial\tilde{\phi}}{\partial x_j}\right)\right]^* dt+S(\phi^*)dt-\Omega_v^*(\phi-\tilde{\phi}^*)dt+S_m^*\,dt. \tag{69}$$

The particle position equation given by Eq. (1) does not change with the Method of Manufactured Solutions. Given Eq. (1) and (69), the particle evolution is implemented using the second order accurate splitting scheme $\mathbb{TM}^s\mathbb{V}^s\mathbb{MRMV}^s\mathbb{M}^s\mathbb{T}$, where $\mathbb{M}^s$ refers to the increment due to the mean source term S_m and $\mathbb{V}^s$ refers to the increment due to the variance source term S_v. Finally, the implementation is verified by investigating the convergence properties in the first and second moments of the scalar against the analytical solutions manufactured by MMS.

4.1. Definition of error

Next, we define a measure of error used for weak convergence studies. The error is measured on the same mesh as the PDF mesh and, typically, multiple independent trials are performed to estimate various statistics. The error is defined based on the volume averaged estimate (over a PDF cell) of the scalar moments and their exact MMS counterparts identical to the definition presented in [38]. Consider T to be the time over which the convergence study is performed and $\langle\cdot\rangle$ to represent volume-averaged quantities. Let $\left\langle\overline{\phi_m^q}\right\rangle_i$ denote the volume-averaged manufactured qth scalar moment (for $q=1$ and 2) at time T in the ith cell and let $\langle\overline{\phi^q}\rangle_{i,k}$ be the corresponding smoothed (with smoothing length scale l) estimate of the qth scalar moment obtained by averaging ϕ^q at the same time T over an ensemble of $N_{i,k}$ particles in the ith cell in the kth trial defined by:

$$\langle\overline{\phi^q}\rangle_{i,k}=\left[\frac{1}{N_{i,k}}\sum_{p=1}^{N_{i,k}}\left(\phi_p^*(T)\right)^q\right]_l. \tag{70}$$

We define the error in the estimated qth scalar moment at time T in the ith cell on the kth trial as,

$$e_{q,i,k}=\langle\overline{\phi_m^q}\rangle_i-\langle\overline{\phi^q}\rangle_{i,k}. \tag{71}$$

A PDF calculation is performed with a finite number of particles and the local error $e_{q,i,k}$ can be approximated to be a random variable with a normal distribution as,

$$e_{q,i,k}=\mu_{q,i}+\sigma_{q,i}\eta_{q,i,k}\quad\text{with} \tag{72}$$

$$\eta_{q,i,k}\overset{D}{=}\mathcal{N}(0,1). \tag{73}$$

The random error $\sigma_{q,i}$ is a measure of the statistical error in the estimate (Eq. 70) and it scales as $N_{\text{pc}}^{-1/2}$ for $l=0$ whereas the deterministic error $\mu_{q,i}$ is comprised of contributions primarily from three sources: spatial discretization error, temporal discretization error and bias error and scales as N_{pc}^{-1} for $l=0$. The smoothing operation incurs an additional smearing error. Un-biased estimates of $\sigma_{q,i}$ and $\mu_{q,i}$ may be constructed from the numerical calculations by considering the mean and the variance of $e_{q,i,k}$ from a finite number of realizations K as [38],

$$\sigma_{q,i}^2\approx\frac{K}{K-1}\left[\left\langle e_{q,i}^2\right\rangle-\langle e_{q,i}\rangle^2\right], \tag{74}$$

$$\mu_{q,i}^2\approx\frac{K}{K-1}\left[\langle e_{q,i}\rangle^2-\frac{1}{K}\left\langle e_{q,i}^2\right\rangle\right], \tag{75}$$

where the expectations $\langle\cdot\rangle$ are obtained by averaging over the K realizations.

We now define the following three global errors with N_{cell} being the total number of cells:

$$\mathcal{E}_{s,q}=\left[\frac{1}{N_{\text{cell}}}\sum_{i=1}^{N_{\text{cell}}}\sigma_{q,i}^2\right]^{\frac{1}{2}}, \tag{76}$$

$$\mathcal{E}_{d,q}=\left[\frac{1}{N_{\text{cell}}}\sum_{i=1}^{N_{\text{cell}}}\mu_{q,i}^2\right]^{\frac{1}{2}}, \tag{77}$$

$$\mathcal{E}_q=\left[\mathcal{E}_{d,q}^2+\mathcal{E}_{s,q}^2\right]^{\frac{1}{2}}=\left[\frac{1}{N_{\text{cell}}}\sum_{i=1}^{N_{\text{cell}}}\left(\mu_{q,i}^2+\sigma_{q,i}^2\right)\right]^{\frac{1}{2}}. \tag{78}$$

The definition of the error given by Eq. (76) is a global measure of the statistical error in the estimate of the qth scalar moment while Eqs. (77) and (78) define the global deterministic error and the root-mean-squared error, respectively. The deterministic global error given by Eq. (77) is the primary measure used to evaluate the accuracy of the various numerical schemes considered in this study while all the three measures of error given by Eqs. (76)–(78) are extensively used in the analysis of the smoothing scheme.

In summary, this section presents the numerical methodologies developed as part of this work for the implementation of the mixing step given by Eq. (2) and its evaluation using MMS, in the context of LES/PDF methods. The following section describes the results obtained from using these schemes in a suite of test problems manufactured using the MMS.

5. Results and discussion

This section is arranged in two subsections. Section 5.1 demonstrates the accuracy of the various implementation methodologies described in Section 3 while Section 5.2 elaborates on the benefits of using smoothing.

5.1. Accuracy and computational cost

Here we present the results that probe the numerical implementation of mixing and molecular transport in the HPDF code for order of accuracy, agreement between the modeled error and the data from numerical tests and computational cost. This section is categorized into three parts: First we present results, for a test case defined in a 3D Cartesian coordinate system (see Appendix D.1), comparing the order of accuracy of the three schemes – PIC-PC, PIC-PL and CIC-LS. Next, we compare the cost incurred by each scheme and finally, the method is verified in a cylindrical coordinate system based on a 3D test problem described in Appendix D.2.

5.1.1. Cartesian – mixing and molecular transport

The implementation of mixing and molecular transport is verified using the MMS for a single scalar. Given $\widetilde{\mathbf{U}}$, $\bar{\rho}$, Γ, Γ_T and Ω_m, analytical solutions are manufactured for the scalar mean $\bar{\phi}_m$ and variance $\overline{\phi'^2}_m$. The details of the test case are described in Appendix D.1. The three numerical schemes: PIC-PC, PIC-PL and CIC-LS are evaluated for accuracy (spatial, temporal and bias errors) in the first two scalar moments using the global error defined by Eq. (77).

First, the three schemes are evaluated with the coefficients U_o, $D_{o,t}$ and R_o taken to be zero. In such a case, the only processes relevant are mixing, molecular transport and the source terms S_m and S_v. The splitting scheme described in Section 3.1 reduces to being $\mathbb{M}^s\mathbb{V}^s\mathbb{M}\mathbb{M}\mathbb{V}^s\mathbb{M}^s$. The normalized smoothing length scale l is set to zero *i.e.*, no smoothing is performed.

Fig. D.4 compares the global error, defined by Eq. (77), in the three schemes PIC-PC, PIC-PL and CIC-LS in terms of accuracy in spatial truncation error, temporal discretization error and bias error in the first two scalar moments. From the sub-Figs. (1a)–(1b) it can be inferred that CIC-LS incurs more error as compared to the two other schemes. The bias error is small as compared to the spatial and temporal errors and is dominated by spatial and temporal discretization error in sub-Figs. (3a)–(3b). The differences between the schemes PIC-PC and PIC-PL are small.

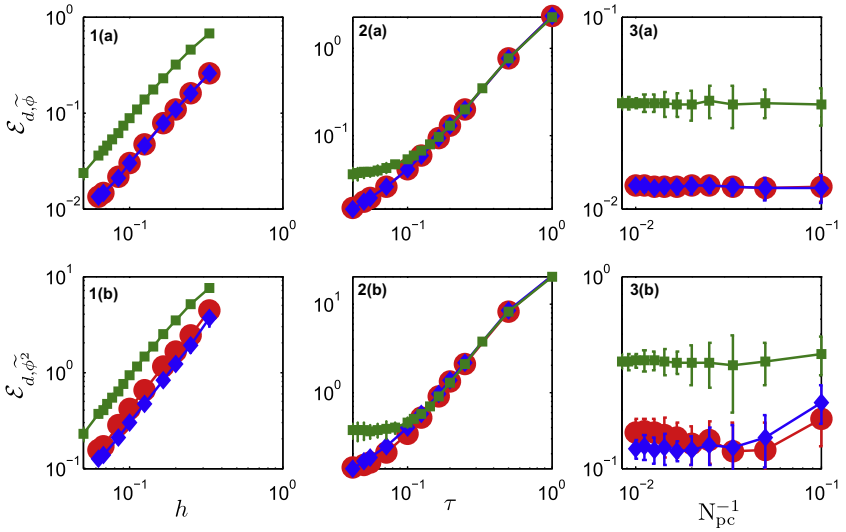

Fig. D.4. Comparison between the three numerical schemes: PIC-PC (circles), PIC-PL (diamonds), CIC-LS (squares) in terms of the estimated global error. The sub-Figs. (1) plot convergence of spatial discretization error, sub-Figs. (2) plot convergence of temporal discretization error, and sub-Figs. (3) plot bias convergence. The sub-figures marked (a) correspond to the convergence for the first scalar moment and those marked (b) to the scalar second moment. The symbols correspond to the data obtained from PDF calculation (refer to Appendix D.1 for test case with U_o, $D_{o,t}$ and R_o taken to be zero).

The deterministic global error in the absence of smoothing is modeled as,

$$\dot{\mathcal{E}}_d = ah^2 + b\tau^2 + \frac{c}{N_{\text{pc}}}, \tag{79}$$

where the first term on the right-hand side represents the spatial truncation error due to finite grid size, $h = \Delta x/L$; the second term models the temporal error due to $\tau = \Delta t/T$; and the final term models the bias error due to a finite number of particles per cell, N_{pc}. The dot '$\cdot$' indicates modeled quantities. Each of the coefficients a, b and c is obtained from a weighted least-squares fit to the data obtained from the calculations. Eq. (79) provides a simple linear model for the deterministic error and is promising for the manufactured problems described here, in the absence of smoothing.

Next, Fig. D.5 compares the global errors incurred by the CIC-LS against the model for that error given by Eq. (79). The symbols are from the PDF calculation and the solid line corresponds to the model for the global error. The sub-figures (a) are at $\tau = 0.03$ and $N_{\text{pc}} = 100$; sub-figures (b) at $h = 0.06$ and $N_{\text{pc}} = 50$; and sub-figures (c) at $h = 0.06$ and $\tau = 0.03$. As can be observed, the model agrees very well with the data showing that the numerical implementation of mixing and molecular transport is second-order accurate in space and time for each of the three numerical methods. The bias error is small in comparison. Similar trends in the agreement between the data and the corresponding error model are observed for the PIC-PC and PIC-PL schemes (not shown here).

Next, Fig. D.6 compares the global error, defined by Eq. (77), incurred by CIC-LS in terms of accuracy in spatial discretization error, temporal discretization error and bias error against the model for that error given by Eq. (79). The test problem is described in Appendix D.1 and models non-trivial transport and reaction with the default values for the U_{o}, $D_{\text{o,t}}$ and R_{o}. The symbols are from the PDF calculation and the solid line corresponds to the model for the global error. The sub-figures (a) are at $\tau = 0.03$ and $N_{\text{pc}} = 100$; sub-figures (b) at $h = 0.06$ and $N_{\text{pc}} = 50$; and sub-figures (c) at $h = 0.1$ and $\tau = 0.05$. As can be observed, the model agrees very well with the data showing that second-order accuracy in space and time is preserved with non-trivial transport and reaction. The bias error in the second moment is significant and the data show that bias error scales as N_{pc}^{-1}.

5.1.2. Computational cost

In this section, we compare the cost of implementing each scheme described in Section 3. Since the only difference in each of these schemes is in the implementation of mixing (mean estimation and interpolation methods), the cost of each scheme is compared by looking at the CPU time per particle step spent on mixing in comparison to the time spent per particle step. The CPU time per particle step of mixing is further split to see the cost of the various mean estimation and interpolation methods. Note that each set of calculations was performed using 32 cores on an HPC cluster of 36 Dell servers, each featuring dual, dual-core 3GHz Intel Xeon "Woodcrest" processors with 8 GB RAM, tied together using a QLogic 4X SDR InfiniBand interconnect.

Fig. D.7 plots the CPU time per particle step (in μs) for each of the three schemes. The figure indicates that the CIC-LS scheme incurs almost three times the cost as either of the other two schemes. This is due to the fact that in CIC-LS, for each particle, the basis functions are evaluated in each of the neighboring 26 cells (in 3D) in addition to one to which the particle

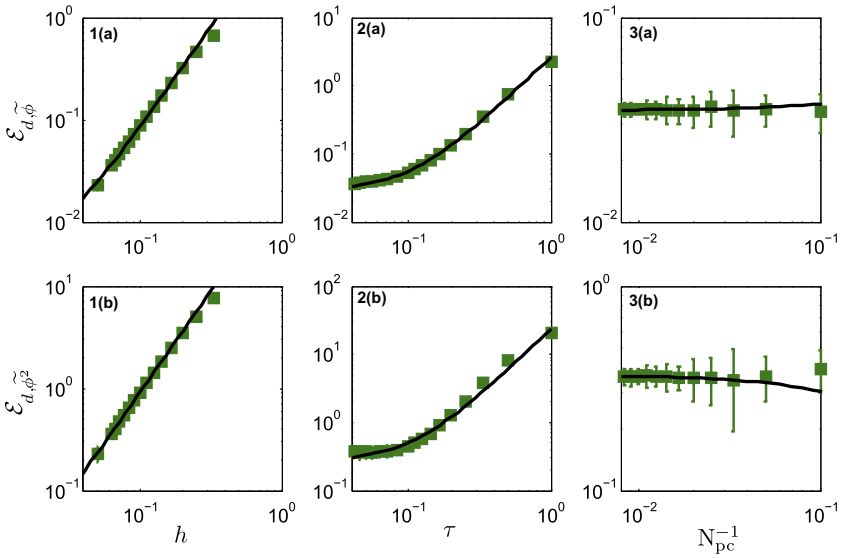

Fig. D.5. Comparison of estimated global error given by Eq. (77) obtained from PDF calculations (refer Appendix D.1 for test case with U_{o}, $D_{\text{o,t}}$ and R_{o} taken to be zero) using the scheme CIC-LS, against the model for the error given by Eq. (79). Details of the sub-figures are identical to the description given in Fig. D.4.

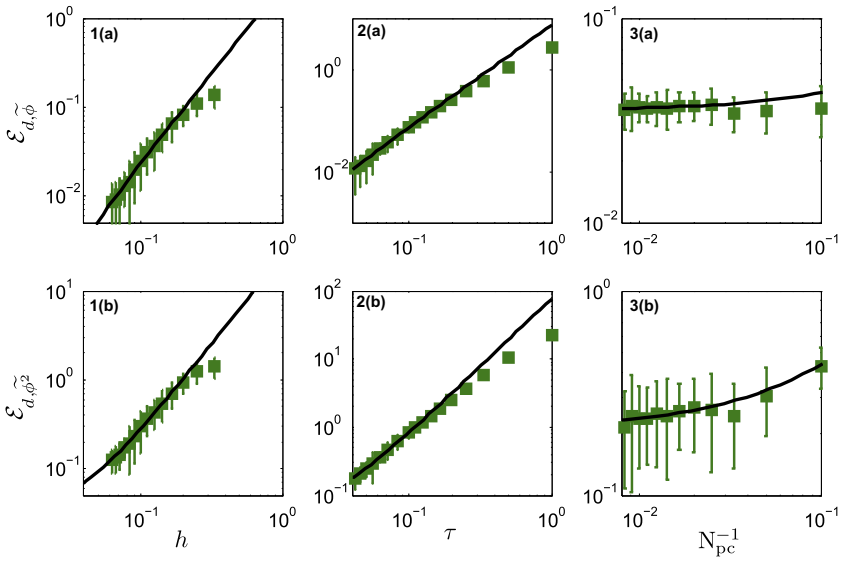

Fig. D.6. Comparison of estimated global error given by Eq. (77) obtained from PDF calculations (refer Appendix D.1 for test case with non-trivial transport and reaction) using the scheme CIC-LS, against the model for the error given by Eq. (79). Details of the sub-figures are identical to the description given in Fig. D.4.

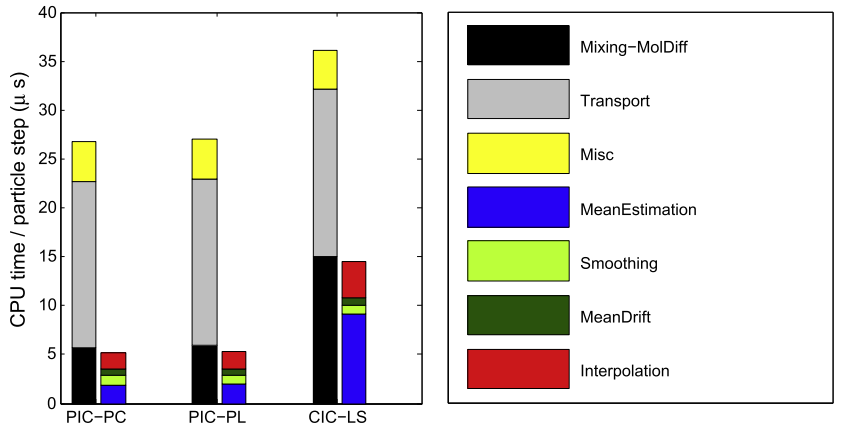

Fig. D.7. Comparison in the computational cost for the three numerical schemes: PIC-PC, PIC-PL and CIC-LS in terms of the CPU time per particle step (in micro seconds). The first stack under each scheme decomposes the cost into mixing $\mathbb{M}$, transport $\mathbb{T}$ and other steps. The second stack decomposes the time spent within mixing $\mathbb{M}$ into mean estimation, smoothing, molecular transport to obtain the mean drifts and interpolation.

belongs. In contrast, in PIC-PC and PIC-PL, the indicator function is evaluated just once per particle. While in these tests the smoothing length-scale is set to zero, nevertheless the smoothing operations are performed (yielding the trivial results $g = f$). This enables the measurement of the CPU time required for smoothing (which is independent of l). As may be seen, the CPU time requirement that pertains to smoothing is modest, amounting to less than 3% of the total for CIC-LS.

The results from the numerical tests presented above indicate that the differences in accuracy across the three schemes for a 3D Cartesian MMS test problem are small. The CIC-LS scheme has two advantages over the other two schemes since the resulting fields are always continuous and bounded. Therefore, although the CIC-LS scheme is relatively expensive in comparison to the other two schemes, we choose the CIC-LS scheme for all the following tests.

5.1.3. Cylindrical – mixing, molecular transport, transport and reaction

In this section, the CIC-LS scheme is evaluated for accuracy in spatial discretization, temporal discretization and bias for the MMS test problem in a cylindrical coordinate system described in Appendix D.2. Fig. D.8 plots the estimate for global error obtained from the PDF calculation against h, τ and N_{pc}^{-1}. The model for the error given by Eq. (79) is plotted so that a comparison can be made between the model predictions and the data from calculations. As is seen from the figure, the

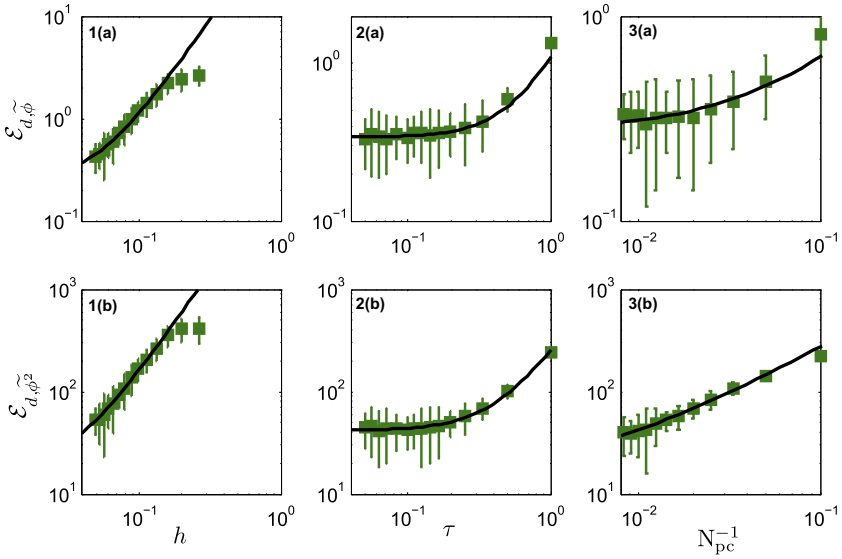

Fig. D.8. Comparison of estimated global error given by Eq. (77) obtained from PDF calculations (refer Appendix D.2 for test case with non-trivial transport and reaction in cylindrical coordinate system) using the scheme CIC-LS, against the model for the error given by Eq. (79). Details of the sub-figures are identical to the description given in Fig. D.4.

implementation is second-order accurate in space and time and the model for the error agrees well with the data for spatial and temporal truncation errors. Additionally, the model for the bias error agrees with the data as well.

In summary, the data from PDF calculations using the MMS testing methodology confirm that the numerical implementation of mixing and molecular transport is second-order accurate in space and time in both the Cartesian and the cylindrical coordinate systems. There are insignificant differences between the three schemes in terms of accuracy, and for reasons mentioned in the previous section, we choose the CIC-LS scheme for all our results henceforth.

5.2. Smoothing

Smoothing, as described in Section 3.4, is presented as a technique for reducing the variance in the estimated statistics by spatial averaging. In this subsection, we study the efficacy of incorporating smoothing by analyzing the behavior of the root-mean-squared error in the estimated statistics of "output" quantities. The test case used is the MMS problem defined in a 3D Cartesian domain (Appendix D.1) without transport and reaction. The numerical scheme used for implementation is the CIC-LS scheme.

As mentioned previously, the root-mean-squared error consists of two components – the deterministic part and the random part. The deterministic error is composed of contributions from (a) spatial truncation error due to finite grid spacing, (b) temporal truncation error due to finite time step, and (c) smearing error due to smoothing. Additionally, using a finite number of particles in the Monte-Carlo particle method gives rise to a deterministic bias error and a random statistical error. Consequently, the fundamental numerical parameters relevant to this study in the analysis of the model for error are the normalized grid spacing h, time step τ, normalized smoothing length scale l, and the total number of particles N_{tot}. The total number of particles, N_{tot}, is chosen to be one of the numerical parameters over the number of particles per cell N_{pc} because the total particle work in a PDF calculation scales with N_{tot}.

Typically, in LES/PDF studies, the choice of the time step is restricted to very small values due to considerations of stability and the CFL number criterion. It has been observed in the jet flame calculations done by Wang and Pope [31] that, for the values of τ used in practice, the temporal error is negligible compared to the contributions from other errors. Likewise, for sufficiently small values of the timestep, the temporal error measured in the numerical studies performed as part of the current work using MMS is negligible. Therefore, we confine our analysis to the 3-D numerical parametric space characterized by h, l and N_{tot}. The MMS calculations are performed for h ranging between 10^{-2} and 1; for l between 0 and 1; and for N_{tot} between 10^3 and 10^7.

Fig. D.9 plots an estimate of the global errors as defined by Eqs. (77 and 78) in the scalar mean and scalar second moment obtained from PDF calculations (shown as symbols) against the smoothing length scale, l for given h and N_{tot}. The normalized grid spacing h is fixed at 0.05 and the total number of particles, $N_{\mathrm{tot}} = 8000$. The filled circles represent the estimate for the global error given by Eq. (77) and correspond to the deterministic error, the filled squares represent the estimate for the global error given by Eq. (76) corresponding to the statistical error and the filled diamonds correspond to the root-mean-squared error given by Eq. (78). It can be inferred that the global estimate for the deterministic error decreases with decreasing l for large l values, reaches a minimum and then increases before leveling off. On the other hand, the global estimate for the statistical error decreases for increasing l. Since the root-mean-squared error is defined to be a combination

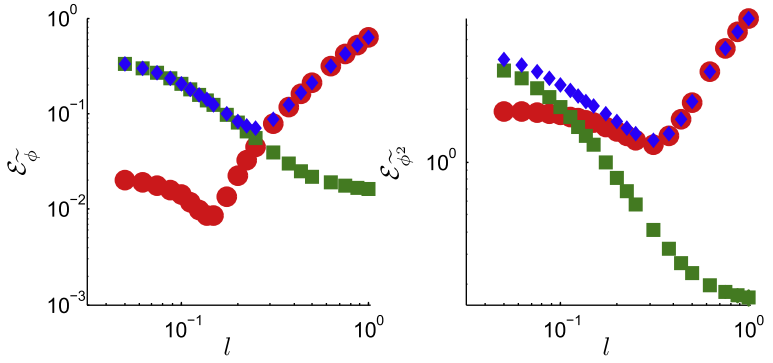

Fig. D.9. Global error in the scalar mean (left) and the second moment (right) against l for fixed $h = 0.05$ and $N_{\text{tot}} = 8000$. Symbols are results of PDF calculations and correspond to $\mathcal{E}_d$ given by Eq. 77 (circle), $\mathcal{E}_s$ given by Eq. 76 (square), $\mathcal{E}$ given by Eq. 78 (diamond).

of the deterministic and statistical errors, there exists a minimum and the corresponding value of l represents optimal smoothing.

We are interested in modeling the root-mean-squared error as a function of the three numerical parameters h, l and N_{tot} across the range of parametric space considered in this study. Consequently, in the following paragraphs, we present models for the statistical error and the deterministic error in terms of h, l and N_{tot} and derive a model for the root-mean-squared error based on these models for the statistical and deterministic errors. While we focus on the scalar mean, the model is itself general and is extensible to any measured statistic.

Considering the statistical error first, we model the global statistical error as

$$\dot{\mathcal{E}}_s = c_0 N_{\text{eff}}^{-\frac{1}{2}}, \tag{80}$$

where the effective number of particles, N_{eff} is defined in Eq. (63). The definition of N_{eff} given by Eq. (63) implies that for $l = 0, N_{\text{eff}} = N_{\text{tot}} h^D = N_{\text{pc}}$ while for $h = 0, N_{\text{eff}} = N_{\text{tot}} l^D$ with $D = 3$. Fig. D.10 presents the estimate of the global statistical error obtained from PDF calculations as symbols and the solid lines to represent the model given by Eqs. (63) and (80) with $c_0 = 0.8$. The sub-Figs. (1) correspond to $N_{\text{tot}} = 8000$; sub-Figs. (2) correspond to $N_{\text{tot}} = 128,000$; and sub-Figs. (3) correspond to $N_{\text{tot}} = 1,638,400$. The figure labels (a) consider the variation of the statistical error with l and (b) consider the variation with h. The primary observation is that the model for the statistical error given by Eq. (80) agrees well with the data across the parametric space explored. It can be inferred that given h, for values of l larger than 10^{-2}, the statistical error is reduced significantly as compared to when no smoothing is performed *i.e.*, for $l = 0$. Similarly, for a given value of N_{tot} with $l = 0$, grid refinement results in the statistical error scaling as $(N_{\text{tot}} h^3)^{-\frac{1}{2}} = N_{\text{pc}}^{-\frac{1}{2}}$ (denoted by the red line). On the other hand, for non-trivial smoothing ($l > 0$), the statistical error asymptotes to a constant given by $c_0 (N_{\text{tot}} l^3)^{-\frac{1}{2}}$. Therefore, we can infer that given N_{tot} and l, as the grid is refined the statistical error scales with $N_{\text{pc}}^{-\frac{1}{2}}$ with no smoothing ($l = 0$) and with $N_{\text{tot}}^{-\frac{1}{2}}$ with non-trivial smoothing ($l > 0$). This is demonstrated by Fig. D.11 which compares the statistical error for various values of h against N_{tot} with smoothing (open symbols, $l > 0$) and without smoothing (filled symbols, $l = 0$) for a fixed value of N_{pc} against the model given by Eq. (80) (solid line).

Next, we examine the data for the estimate of the global deterministic error in Fig. D.12. The sub-figure (a) plots the deterministic error against l at a given value of h for the three values of N_{tot} while (b) plots against h at a given value of l for the same three values of N_{tot}. The data show no dependence on N_{tot} indicating that the bias error is negligible in comparison to the smearing and spatial discretization errors. A striking feature of the plot of $\mathcal{E}_d$ vs. l (Fig. D.12) is the sharp minimum around $l \approx 0.5$, for which we offer the following explanation.

Prior to smoothing, the deterministic error is dominated by spatial truncation error and as mentioned previously, smoothing introduces additional smearing errors. Smoothing tends to smear both the underlying field (which is undesirable) and the spatial truncation error (which is desirable). For small values of the smoothing length scale $l \leqslant h$, the smearing error is smaller or comparable to the spatial truncation error. As we increase the smoothing length scale, there exists an optimal value of l at which the smearing of the underlying field is compensated for by the smearing of the spatial truncation error, resulting in a minimum deterministic error. This behavior is well portrayed in the left-hand plot of Fig. D.12.

Appendix B.2 analyzes the smearing error incurred due to smoothing and presents approximate models for the same in Eqs. (B.23) and (B.24) for two specific cases (see the appendix for details). This analysis is used to suggest a form for a model of the deterministic error incurred after smoothing, and we accordingly model the global deterministic error as:

$$\begin{aligned}\dot{\mathcal{E}}_d^2 &= \left(\frac{\dot{a}_1 \alpha_s h^2 - \dot{a}_2 h^2}{1 + \dot{a}_5 \alpha_s h^2}\right)^2 + \left(\frac{\dot{a}_4 h^2}{1 + \dot{a}_3 \alpha_s}\right)^2, \\ &= \left(\frac{a_1 l^2 - a_2 h^2}{1 + a_5 l^2}\right)^2 + \left(\frac{a_4 h^4}{h^2 + a_3 l^2}\right)^2,\end{aligned} \tag{81}$$

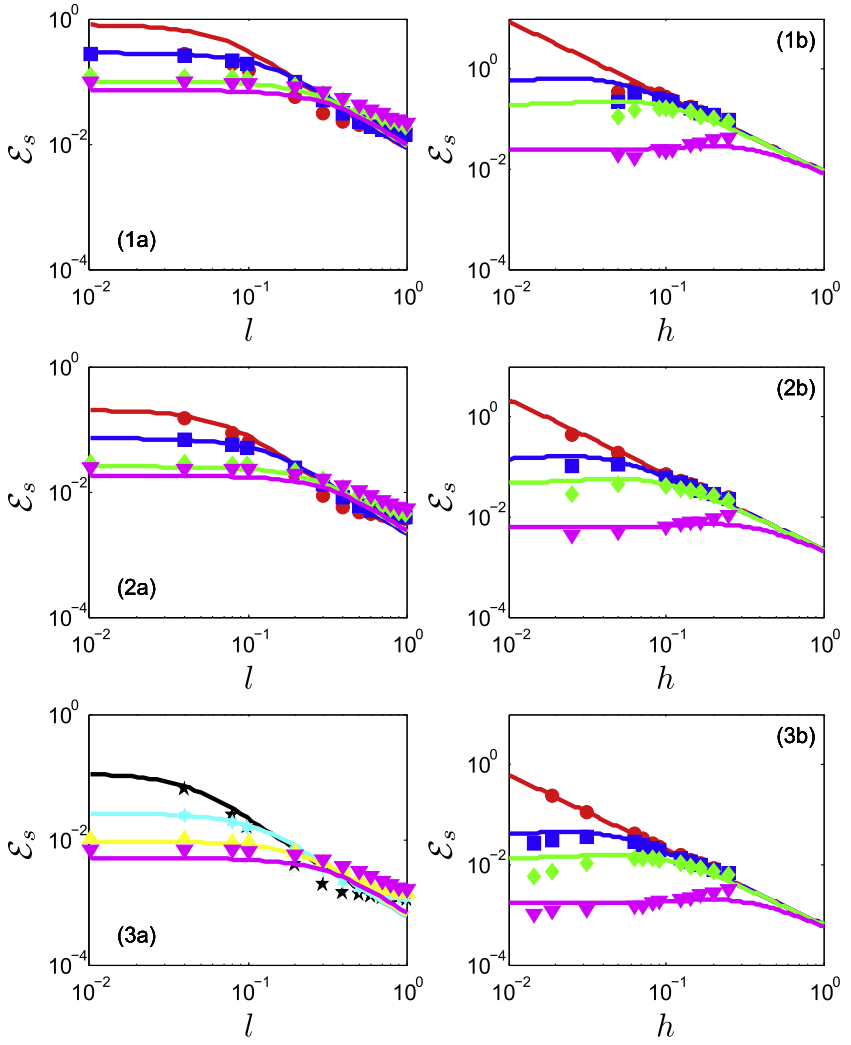

Fig. D.10. Comparison between the estimate of the global statistical error in the scalar mean obtained from the PDF calculations (symbols) and its model given by Eq. (80). Sub-Figs. (1) are at $N_{\text{tot}} = 8000$, (2) at $N_{\text{tot}} = 128,000$ and (3) at $N_{\text{tot}} = 1,638,400$. Sub-figures (a) plot against l for fixed h (note that data for $l = 0$ is in fact plotted at $l = 10^{-2}$) and (b) plots against h given l. Plots under sub-figures (a) follow the legend: $h = 0.05$ (circles), $h = 0.1$ (squares), $h = 0.2$ (diamonds), $h = 0.25$ (inverted triangles), $h = 0.03125$ (stars), $h = 0.083$ (hexagons), $h = 0.16$ (triangles). Plots under sub-figures (b) follow the legend: $l = 0$ (circles), $l = 0.5$ (squares), $l = 0.125$ (diamonds), $l = 0.0625$ (inverted triangles).

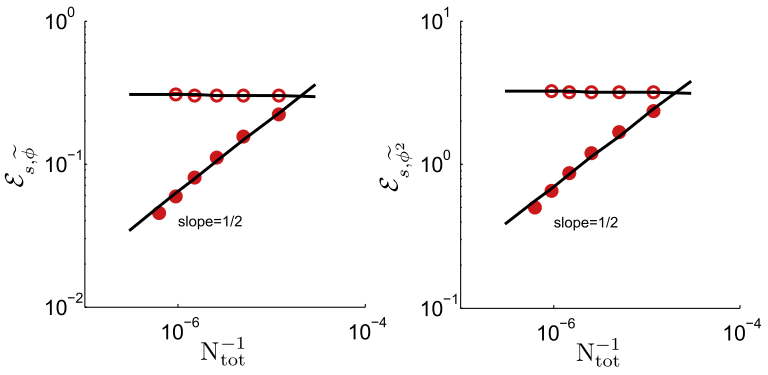

Fig. D.11. Statistical error in the scalar mean and the second moment against N_{tot}^{-1} for fixed N_{pc}. Symbols are results of PDF calculations. Solid lines correspond to the model for the global error given by Eq. (80). Symbols : $l = 0.04$ (filled circles) and $l = 0$ (open circles).

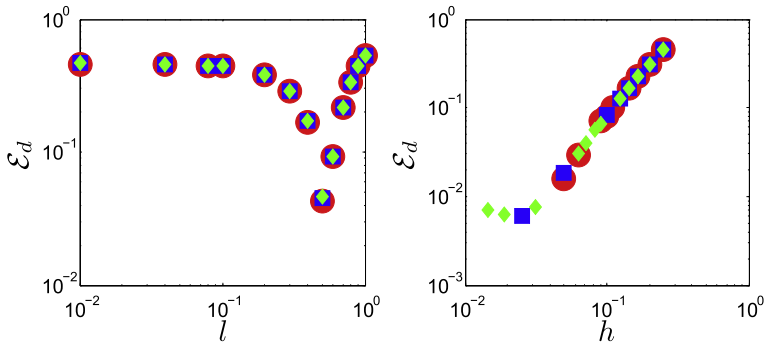

Fig. D.12. Comparison between the estimate of the global deterministic error in the scalar mean obtained from the PDF calculations against l for $h = 0.25$ and against h for $l = 0.0625$. Symbols: $N_{\text{tot}} = 8000$ (circles), $N_{\text{tot}} = 128,000$ (squares), $N_{\text{tot}} = 1,638,400$ (diamonds).

where the second line is obtained using Eq. (55) as a model for α_s and a_i are empirical constants. Fitting the model given by Eq. (81) to the data for the estimate of the deterministic error obtained from PDF calculations, we obtain $a_1 = 1.52,\ a_2 = 7.27,\ a_3 = 0.75,\ a_4 = 1.76$ and $a_5 = 0.98$.

Fig. D.13 plots the deterministic error against l in sub-figures marked (a) and against h in sub-figures marked (b) for the three values of N_{tot} values. The data from PDF calculations correspond to the symbols and the lines represent the model given by Eq. (81). The model is successful in predicting the behavior exhibited by the data across the range of parameters studied. In particular, in most cases, the model prediction of location of the optimal error is in good agreement with the data.

Given the models for the statistical error in Eq. (80) and the deterministic error in Eq. (81), the model for the global estimate of the corresponding root-mean-squared error is obtained as,

$$\dot{\mathcal{E}}^2 = \dot{\mathcal{E}}_d^2 + \dot{\mathcal{E}}_s^2. \tag{82}$$

Fig. D.14 compares the model given by Eq. (82) against the data from PDF calculations for the three values of N_{tot} analyzed. As is evident, the model agrees well with the PDF simulations and is successful in predicting their behavior quantitatively. As with the deterministic error, the model for the root-mean-squared error is successful in predicting the location of the optimal error.

The deterministic error given by Eq. (81) is modeled based on the analysis performed in Appendix B.2 for the smearing error due to smoothing. Consider making the following approximation to Eq. (81) where we force the coefficient a_5 (in Eq. (81)) to zero to obtain:

$$\dot{\mathcal{E}}_d^2 = (c_1 l^2 - c_2 h^2)^2 + \left(\frac{c_4 h^4}{h^2 + c_3 l^2}\right)^2 \tag{83}$$

for a different set of coefficients c_i. The motivation behind this approximation becomes clear in the following paragraphs. Note that this approximation likely tends to affect choices of smoothing length scale on the order of unity. Smoothing length scale l of unity implies that smoothing is performed over the entire computational domain.

Fitting this model given by Eq. (83) to the data for the estimate of the deterministic error obtained from PDF calculations, we obtain $c_1 = 0.82,\ c_2 = 3.89,\ c_3 = 0.49$ and $c_4 = 6.45$. Fig. D.15 compares the root-mean-squared error obtained using the models for the deterministic error given by Eq. (81) (thin solid lines) and (83) (thick dashed lines). The discrepancy between the two models are observed for values of l comparable to unity. Barring this drawback, the model corresponding to Eq. (83) yields to elegant inferences as shown below.

Our studies show that the computing time is dominated by particle work and therefore we model the cost, $\mathcal{C}$ to scale with N_{tot}. We now use the model Eq. (83) in the definition of the global root-mean-squared error Eq. (82) to investigate the selection of the optimal value of l. We write this error as $\dot{\mathcal{E}}(h, l, N_{\text{tot}})$ and, as a preliminary step we define $\hat{h}(N_{\text{tot}})$ to be the optimal normalized grid spacing when no smoothing is used, and $\hat{l}(N_{\text{tot}})$ to be the optimal amount of smoothing on an infinitely fine grid. Thus, $\hat{h}(N_{\text{tot}})$ is the minimizer of $\dot{\mathcal{E}}(h, 0, N_{\text{tot}})$, and this minimum error is denoted by $\dot{\mathcal{E}}_h(N_{\text{tot}}) = \dot{\mathcal{E}}(\hat{h}, 0, N_{\text{tot}})$. Similarly $\hat{l}(N_{\text{tot}})$ is the minimizer of $\dot{\mathcal{E}}(0, l, N_{\text{tot}})$ and this minimum error is denoted by $\dot{\mathcal{E}}_l(N_{\text{tot}}) \equiv \dot{\mathcal{E}}(0, \hat{l}, N_{\text{tot}})$. A simple analysis of Eq. (82) obtained using Eqs. (80) and (83) shows that,

$$\hat{h} = \left(\frac{N_{\text{tot}}}{\widetilde{N}_h}\right)^{-q}, \tag{84}$$

$$\hat{l} = \left(\frac{N_{\text{tot}}}{\widetilde{N}_l}\right)^{-q} \tag{85}$$

with $\widetilde{N}_h = c_0^2 D/4c^2$ for $c^2 \equiv c_2^2 + c_4^2$, $\widetilde{N}_l = c_0^2 D/4c_1^2$, and $q^{-1} = 4 + D$. Thus, $\hat{h}$ and $\hat{l}$ decrease at the same slow rate with increasing N_{tot}, as $N_{\text{tot}}^{-1/7}$ for $D = 3$.

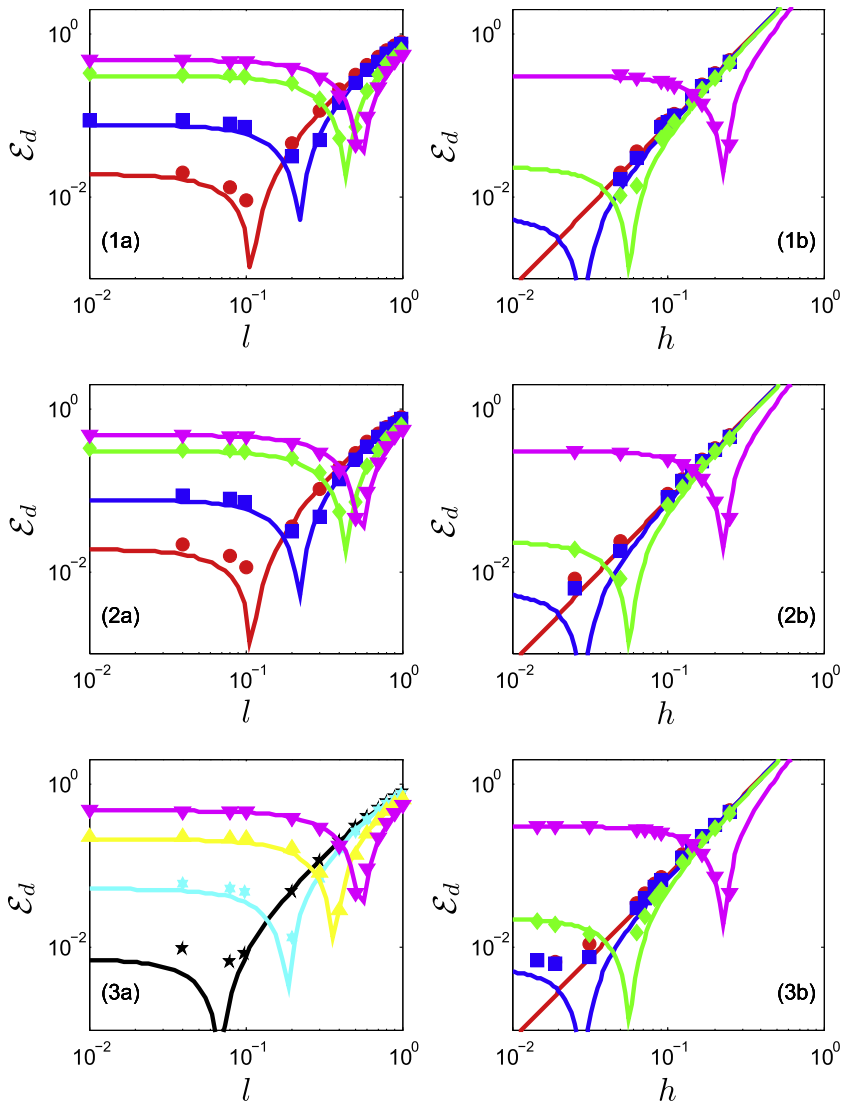

Fig. D.13. Comparison between the estimate of the global deterministic error in the scalar mean obtained from the PDF calculations (symbols) and its model given by Eq. (81). The figure description is the same as in Fig. D.10.

Now, given the definitions of $\hat{l}$ and $\hat{h}$ above, Eqs. (80) and (83) can be re-expressed in terms of $\tilde{l} \equiv l/\hat{l}$ and $\tilde{h} \equiv h/\hat{h}$ to obtain for the root-mean-squared error an expression of the form:

$$\dot{\mathcal{E}}^2 = N_{\text{tot}}^{-4q} \mathcal{F}(\tilde{l}, \tilde{h}) \tag{86}$$

for the set of coefficients c_i where with $r \equiv (c_1/c)^{2q}$ we have,

$$\mathcal{F} = c_0^2 \tilde{N}_l^{-qD} \left(\tilde{h} r + \frac{\tilde{l}^2}{\sqrt{16 r^2 \tilde{h}^2 + \tilde{l}^2}} \right)^{-D} + \tilde{N}_l^{4q} \left[(c_1 \tilde{l}^2 - c_2 r^2 \tilde{h}^2)^2 + \left(\frac{c_4 r^4 \tilde{h}^4}{r^2 \tilde{h}^2 + c_3 \tilde{l}^2} \right)^2 \right]. \tag{87}$$

In other words, $\dot{\mathcal{E}} N_{\text{tot}}^{2q}$ is known completely in terms of the parameters $\tilde{h}$ and $\tilde{l}$ given the coefficients c_i.

Fig. D.16 plots the filled contours of $\log_{10}(\dot{\mathcal{E}} N_{\text{tot}}^{2q})$ in $\tilde{h}$–$\tilde{l}$ space using model coefficients c_i estimated using the data from PDF calculations. Note that $\tilde{l} = 1$ and $\tilde{h} = 1$ are special values. Let $\mathcal{F}_{\min}(\tilde{h})$ be the minimum value of $\mathcal{F}$ over all $\tilde{l}$ *i.e.*,

$$\mathcal{F}_{\min}(\tilde{h}) = \min_{\tilde{l}} \mathcal{F}(\tilde{l}, \tilde{h}), \tag{88}$$

and let $\tilde{l}_{\min}$ be defined such that

$$\mathcal{F}_{\min}(\tilde{h}) = \mathcal{F}(\tilde{l}_{\min}, \tilde{h}). \tag{89}$$

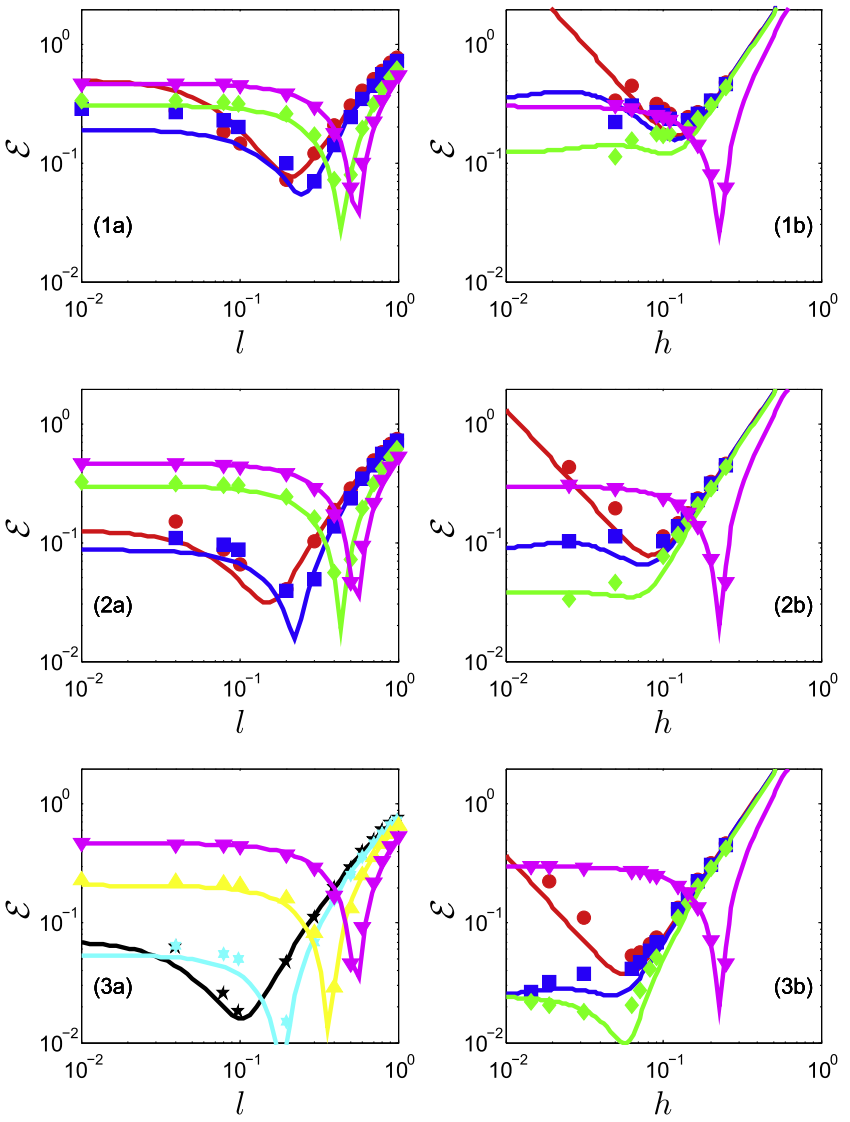

Fig. D.14. Comparison between the estimate of the global root-mean-squared error in the scalar mean obtained from the PDF calculations (symbols) and its model given by Eq. (82). The figure description is the same as in Fig. D.10.

Further let us define $\mathcal{F}_o$ to be the global minimum over all $\tilde{l}$ and $\tilde{h}$. The following observations can be made.

First, consider Fig. D.17(a) which plots the variation of $\tilde{l}_{\min}$ against $\tilde{h}$. For $\tilde{h}$ tending to zero, the optimal error is obtained at $\tilde{l} = 1$. Next, for all values of $\tilde{h} \leqslant 1$, $\tilde{l} = 1$ is a reasonable choice for minimizing the error. For values of $\tilde{h}$ greater than unity, $\tilde{l}$ is directly proportional to $\tilde{h}$. Secondly, consider Fig. D.17(b) which plots $\mathcal{F}_{\min}/\mathcal{F}(0,\tilde{h})$ against $\tilde{h}$ suggesting that given N_{tot} and $\tilde{h}$, the minimum root-mean-squared error in an estimated statistic $\mathcal{F}_{\min}$ after smoothing with $\tilde{l}_{\min}$ is smaller than the error incurred $\mathcal{F}(0,\tilde{h})$ before smoothing is performed. The error is reduced significantly for $\tilde{h} < 1$. In other words, smoothing with an appropriate value of $\tilde{l}$ is always beneficial. Finally, Fig. D.17(c) indicates that to a good approximation, the global minimum $\mathcal{F}_o$ occurs at $\tilde{h} = 1$ and $\tilde{l} = 1$. For $\tilde{h} < 1$, $\mathcal{F}_{\min}$ is approximately 26% larger than $\mathcal{F}_o$. For large $\tilde{h}$ (compared to unity) values, $\mathcal{F}_{\min}$ is proportional to $\tilde{h}$. Moreover, for a value of N_{tot} infinitely large, provided that $\tilde{l}$ and $\tilde{h}$ are chosen such that $\mathcal{F}$ is essentially constant, then

$$\dot{\mathcal{E}} \sim N_{\text{tot}}^{-2q} = N_{\text{tot}}^{-2/7} \text{ in 3D.} \tag{90}$$

Finally, contrasting smoothing with increased kernel widths used for mean estimation, we note the following. Increasing the kernel widths is qualitatively similar to smoothing but smoothing has two advantages. First, the cost of smoothing is independent of the choice of the smoothing length scale, l whereas the cost of kernel estimation increases with the size of the kernel. Secondly, given N_{tot} (or equivalently, the computational cost) and statistical error, the smearing error incurred

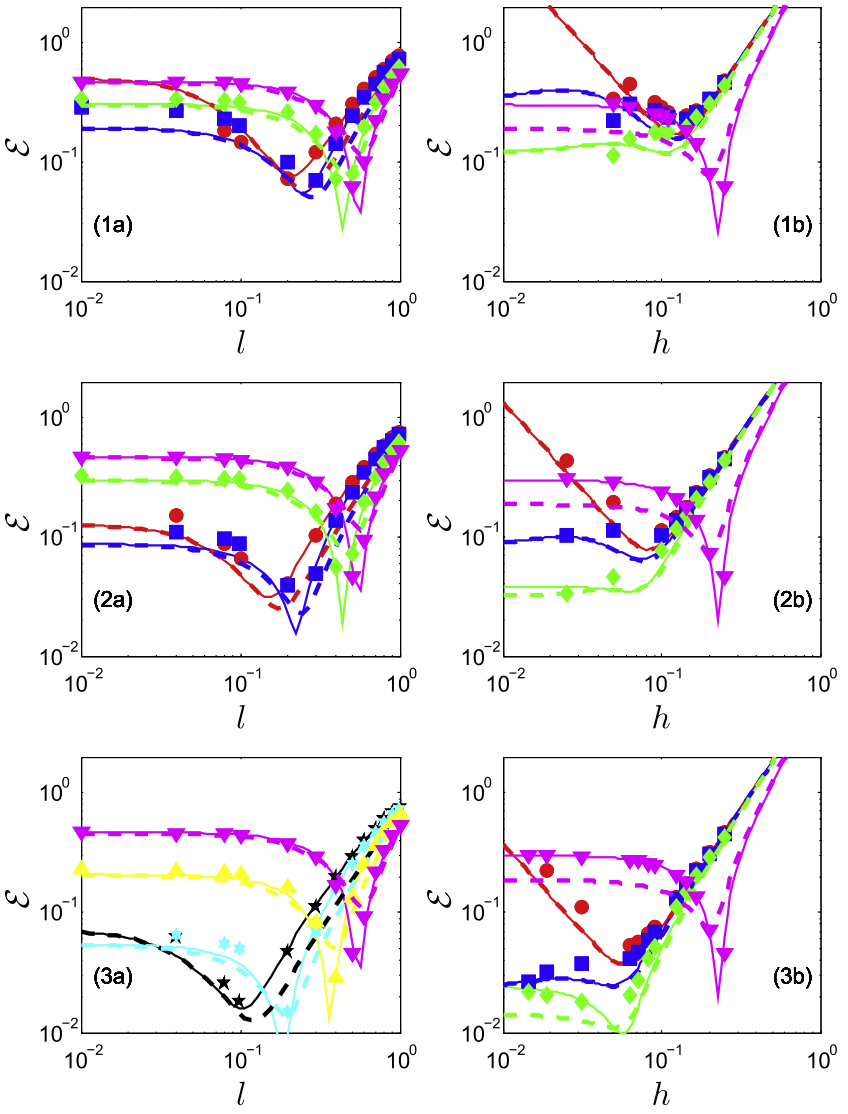

Fig. D.15. Comparison between the estimates of the global root-mean-squared error in the scalar mean obtained from the PDF calculations (symbols) against the root-mean-squared error modeled based the two models for the deterministic error corresponding to Eqs. (81) (thin solid lines) and (83) (thick dashed lines). The figure description is the same as in Fig. D.10.

in smoothing is less than that in kernel estimation. This is demonstrated by Fig. D.18 which compares the modeled statistical error given by Eq. (80) against the deterministic error modeled by Eq. (81) for $N_{\text{tot}} = 128,000$ and various choices of the smoothing length l.

A significant portion of the error analysis and modeling detailed in this paper has been performed and corroborated using the method of manufactured solutions for the specific problem described in Appendix D.1 with no transport or reaction. However, this modeling strategy may be extended to the estimation of errors in other test cases or in a large-eddy simulation. Since, N_{tot} is proportional to the computational cost and the choice of h in a large-eddy simulation determines the total amount of energy resolved, we have shown that given N_{tot} and h, a model for the error similar in form to Eq. (82) provides a reasonable choice for the smoothing length scale l.

In summary, the results suggest the following. Smoothing can be used for two purposes. It can be applied to quantities that are estimated primarily for output purposes. Or it can be applied to quantities that are fed back into the PDF calculations as coefficients of SDEs. Smoothing output quantities reduces the statistical error in their estimate and the error with smoothing scales as $N_{\text{tot}}^{-1/2}$ instead of as $N_{\text{pc}}^{-1/2}$. When smoothing is applied to feedback quantities, it is evident that the bias error now scales as N_{tot}^{-1} instead of N_{pc}^{-1}. An appropriate amount of smoothing is also beneficial in reducing the deterministic error incurred. Therefore, smoothing allows us to decrease the root-mean-squared error incurred for an appropriate choice of the smoothing length scale, l given a total number of particles N_{tot} and h.

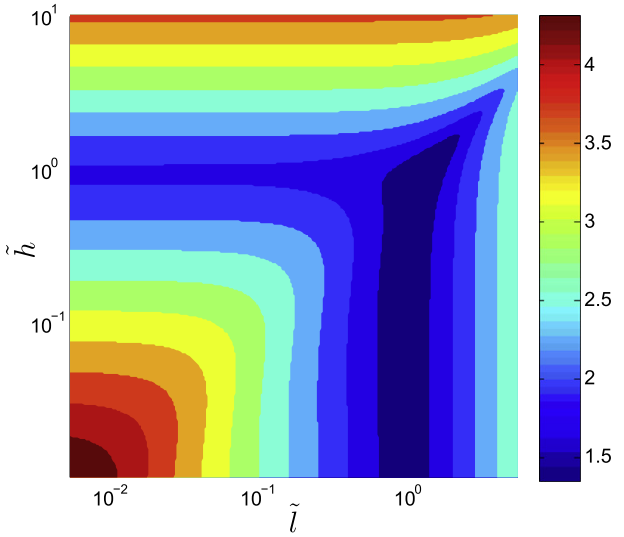

Fig. D.16. Contours of the modeled error $\log_{10}\left(\dot{\mathcal{E}}N_{\text{tot}}^{2q}\right)$ given by Eq. (86) in $\tilde{h}$–$\tilde{l}$ space.

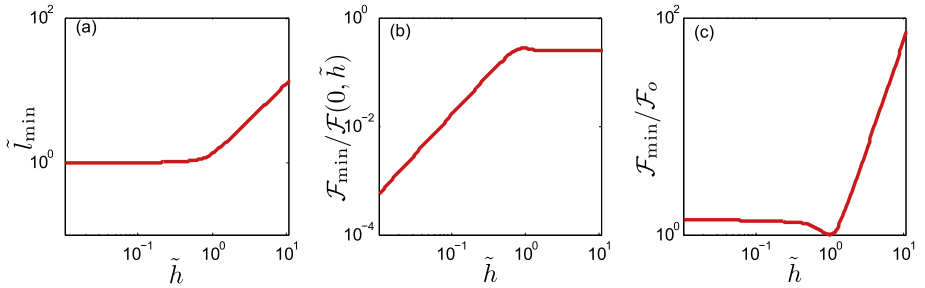

Fig. D.17. (a) Variation of $\tilde{l}_{\min}$ given by Eq. (89) against $\tilde{h}$, (b) variation of $\mathcal{F}_{\min}/\mathcal{F}(0,\tilde{h})$ (Eq. (88)) with $\tilde{h}$ and (c) variation of $\mathcal{F}_{\min}/\mathcal{F}_o$ with $\tilde{h}$.

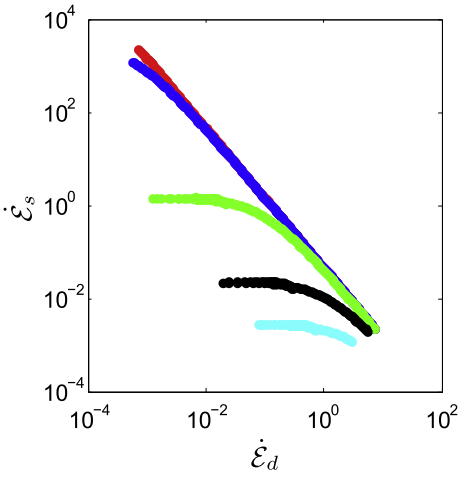

Fig. D.18. Statistical error modeled by Eq. (80) against the deterministic error given by Eq. (81) for fixed $N_{\text{tot}} = 128,000$. Symbols: $l = 0$ (red), $l = 0.01$ (blue), $l = 0.125$ (green), $l = 0.5$ (black) and $l = 1$ (cyan). (For interpretation of the references to color in this figure legend, the reader is referred to the web version of this article.)

6. Differential diffusion

Many mixing and combustion models in turbulence make the assumption of equal molecular diffusivities of all species. This may be justified when the molecular diffusivity is smaller than the turbulent diffusivity. However, in a DNS this assumption is not justified, and in LES/PDF methods, the DNS limit is significant. Sutherland *et al.* [43] analyzed spatially-filtered DNS data of $CH_4/H_2/N_2$ – air and $CO_4/H_2/N_2$ – air flames to show that the importance of differential diffusion increases as the filter size decreases. Kemenov and Pope [30] show from LES studies of a laboratory-scale jet flame (Sandia flame D) that molecular diffusivity is dominant in the near-field of the jet in comparison to the subgrid-scale turbulent diffusivity on reasonably sized grids. The equal diffusivity assumption in such cases might lead to inaccurate predictions for various statistics of interest. In this section, we study the ability of the modified IEM mixing model to account for the effects of differential diffusion.

The current section is organized as follows. In Section 2, it was shown that the mixing model given by Eq. (2) has the capability to account for the effects of differential diffusion. Here, in sub-section 6.1, we extend the mixing model given by Eq. (2) to multiple scalars with equal diffusivities. The modified form of Fick's law is briefly mentioned in Section 6.2. Following this, an extension to multiple scalars with differential diffusion is made in Section 6.3 with the results of a test case that considers mixing of three species with different diffusivities presented in Section 6.4.

6.1. Multiple scalars with equal diffusivities

Consider a PDF calculation of a non-reacting turbulent flow with n_s species each with the same molecular diffusivity $\Gamma(\mathbf{x},t)$. Then, the mixing model given by Eq. (2) can simply be extended to this case of multiple species as,

$$\frac{d\phi_\alpha^*(t)}{dt} = -\Omega_m^*\left(\phi_\alpha^* - \tilde{\phi}_\alpha^*\right) + \left[\frac{1}{\bar{\rho}}\frac{\partial}{\partial x_j}\left(\bar{\rho}\Gamma\frac{\partial\tilde{\phi}_\alpha}{\partial x_j}\right)\right]^*, \tag{91}$$

where ϕ_α for $\alpha = 1,2,\ldots,n_s$ is the set of species mass fractions. It should be noted that the above Eq. (91) is easily obtained by replacing ϕ in Eq. (2) with ϕ_α.

Given that ϕ_α is the set of species mass fractions, a mixing model should satisfy the normalization condition on mass fractions $\sum_\alpha \phi_\alpha = 1$. Now, let $\phi^o = \mathbf{\Theta}^T\boldsymbol{\phi}$, where $\mathbf{\Theta}$ is any constant and uniform vector. Then it is evident that ϕ^o also satisfies Eq. (91). Note that $\mathbf{\Theta}$ can be chosen so that ϕ^o represents conserved quantities: element mass fractions, mixture fractions and the sum of species mass fractions (=1). If ϕ^o is initially constant and uniform, then its value does not change both according to Eq. (91) and in any numerical implementation that guarantees boundedness (since $\min\{\phi^o\} = \max\{\phi^o\}$). Thus the normalization condition on mass fractions is satisfied.

6.2. Modified Fick's law

For a non-reacting flow with n_s species and unequal molecular diffusivities, we consider molecular diffusion to be represented by a modified form of Fick's law in which the diffusion velocity $\mathbf{V}_\alpha$ of species α is given by

$$\phi_{(\alpha)}(V_{(\alpha)j} + V_{cj}) = -\Gamma_{(\alpha)}\frac{\partial\phi_{(\alpha)}}{\partial x_j}, \tag{92}$$

where $\Gamma_\alpha(\mathbf{x},t)$ is the mixture-averaged diffusivity of species α, and $\mathbf{V}_c$ is the correction velocity [44,45] given by,

$$V_{cj} = -\sum_{\alpha=1}^{n_s}\Gamma_\alpha\frac{\partial\phi_\alpha}{\partial x_j}. \tag{93}$$

The suffixes in parentheses are excluded from the summation convention. The correction velocity is thus defined so that the Fick's law model for the mass-averaged diffusion velocity is zero, and therefore the sum of the species mass fraction equations correctly reduces to the mass conservation equation.

6.3. Multiple scalars with unequal diffusivities

For the case of multiple species with unequal molecular diffusivities $\Gamma_\alpha(\mathbf{x},t)$, a mixing model is defined that is consistent with the modified Fick's law:

$$\frac{d\phi_\alpha^*(t)}{dt} = -\Omega_m^*\left(\phi_\alpha^* - \tilde{\phi}_\alpha^*\right) + \left[\frac{1}{\bar{\rho}}\frac{\partial}{\partial x_j}\left(\bar{\rho}\Gamma_{(\alpha)}\frac{\partial\tilde{\phi}_\alpha}{\partial x_j}\right)\right]^* - \left[\frac{1}{\bar{\rho}}\frac{\partial\bar{\rho}\tilde{\phi}_\alpha V_{cj}}{\partial x_j}\right]^*. \tag{94}$$

It should be noted that Eq. (94) differs from Eq. (91) in the last two terms on its right-hand side: the second term involves Γ_α in place of a single diffusivity Γ for all species, and the final term includes the correction velocity $\mathbf{V}_c$. It is evident that given ϕ^o denotes the sum of species mass fractions (=1), ϕ^o satisfies Eq. (94), indicating that the mixing model given by Eq. (94) satisfies the normalization condition on mass fractions. Realizability of species mass fractions is guaranteed when $\phi_\alpha \geqslant 0$

for each α in addition to the normalization condition. Boundedness ($\phi_\alpha \geqslant 0$) can be imposed by fixing a lower limit on the mixing frequency [29] the details of which are presented in Appendix C.

Let us consider the transport equations for the first two scalar moments – the mean and the variance of mass fractions. The transport equation for any scalar moment can be derived from the corresponding PDF transport equation. The modeled PDF transport equation that corresponds to Eqs. (1) and (94) is obtained as,

$$\frac{\partial f_\phi}{\partial t}+\frac{\partial}{\partial x_j}\left[f_\phi\left(\widetilde{U}_j+\frac{1}{\bar\rho}\frac{\partial \bar\rho \Gamma_T}{\partial x_j}\right)\right]=\frac{\partial^2(\Gamma_T f_\phi)}{\partial x_j \partial x_j}+\frac{\partial}{\partial \psi_\alpha}[f_\phi \Omega_m(\psi_\alpha-\tilde\phi_\alpha)]-\frac{\partial}{\partial \psi_\alpha}\left[f_\phi \frac{1}{\bar\rho}\frac{\partial}{\partial x_j}\left(\bar\rho \Gamma_{(\alpha)}\frac{\partial \tilde\phi_\alpha}{\partial x_j}\right)\right]+\frac{\partial}{\partial \psi_\alpha}\left[f_\phi \frac{1}{\bar\rho}\frac{\partial}{\partial x_j}(\bar\rho \tilde\phi_\alpha V_{cj})\right]. \tag{95}$$

First, we consider the transport equation for the first moment of the scalar $\tilde\phi_\alpha$:

$$\frac{\partial \bar\rho \tilde\phi_\alpha}{\partial t}+\frac{\partial \bar\rho \widetilde{U}_j \tilde\phi_\alpha}{\partial x_j}=\frac{\partial}{\partial x_j}\left[\bar\rho(\Gamma_T+\Gamma_{(\alpha)})\frac{\partial \tilde\phi_{(\alpha)}}{\partial x_j}\right]-\frac{\partial}{\partial x_j}[\bar\rho \tilde\phi_\alpha V_{cj}]. \tag{96}$$

Given Eq. (93) and realizable initial and boundary conditions, Eq. (96) guarantees

$$\frac{D}{Dt}\sum_\alpha \tilde\phi_\alpha = 0, \tag{97}$$

where D/Dt is the substantial derivative following a particle and $\tilde\phi_\alpha \geqslant 0$. It should be noted that $\tilde\phi_\alpha \geqslant 0$ and $\sum_\alpha \tilde\phi_\alpha = 1$ implies $\tilde\phi_\alpha \leqslant 1$. Thus, the mixing model given by Eq. (94) guarantees realizability and boundedness of mean mass fractions. The transport equation for the scalar variance remains unchanged from Eq. (8) (with $S = 0$) *i.e.*, according to the model, the variances are not directly affected by molecular diffusivities.

The following paragraphs detail an algorithm for the numerical implementation of Eq. (94). Given the pair of equations Eqs. (1) and (94), we adopt a splitting scheme of type $\mathbb{TMRMT}$ to solve for particle transport $\mathbb{T}$, mixing $\mathbb{M}$ and reaction $\mathbb{R}$. While the mixing step was split into IEM mixing step $\mathbb{I}$ and estimation of mean drifts due to molecular transport $\mathbb{D}$ as $\mathbb{IDI}$ in Section 3.1 for the case of equal diffusivities, with differential diffusion we adopt a scheme denoted as $\mathbb{IDCI}$ for the mixing step where $\mathbb{C}$ denotes the correction imposed to satisfy the normalization condition on species mass fractions (corresponding to Eq. (93)). It should be noted that the mixing step given by the splitting scheme $\mathbb{IDCI}$ is not symmetric and therefore, the overall scheme reduces to first-order temporal accuracy in the presence of differential diffusion.

The one-step update for the particle scalar with differential diffusion is numerically implemented similar to Eq. (18) for a single scalar as:

$$\phi_\alpha^{*,n+1}=\phi_\alpha^{*,n}+c^{*,n+\frac{1}{2}}\left(\tilde\phi_\alpha^{*,n}-\phi_\alpha^{*,n}\right)+\Delta\tilde\phi_\alpha^{*,n+\frac{1}{2}} \tag{98}$$

with the mean drift $\Delta\tilde\phi_\alpha$ now defined in terms of the change in solution over a time-step of the heat conduction equation $\Delta\tilde\phi_\alpha^h$ and the correction to the mean drift $\Delta\tilde\phi_\alpha^c$ as,

$$\Delta\tilde\phi_\alpha^{*,n+\frac{1}{2}}\equiv\Delta\tilde\phi_\alpha^{h,*,n+\frac{1}{2}}-\Delta\tilde\phi_\alpha^{c,*,n+\frac{1}{2}}. \tag{99}$$

Note that $\Delta\tilde\phi_\alpha^{h,*,n+\frac{1}{2}}$ is the change in the solution over one time-step, in species α estimated at particle locations, obtained using Eq. (4) given $\tilde\phi_\alpha^n$ and $\Delta\tilde\phi_\alpha^{c,*,n+\frac{1}{2}}$ is the correction to the mean drift and is obtained as the change in solution to

$$\frac{\partial \bar\rho \tilde\phi_\alpha}{\partial t}=\frac{\partial \bar\rho \tilde\phi_\alpha V_{cj}}{\partial x_j}, \tag{100}$$

over the same time-step given $\tilde\phi_\alpha^n$ and $\mathbf{V}_c^{n+\frac{1}{2}}$. The precise details of the numerical implementation are provided in Appendix A. In Appendix C, it is shown that this numerical implementation satisfies conservation and realizability.

In summary, we present a model for scalar mixing that incorporates differential diffusion effects correctly. A splitting scheme is presented that satisfies conservation and realizability constraints (shown in Appendix C) but reduces to first-order temporal accuracy in the presence of differential diffusion. The following section analyzes this model and its implementation using a three-species mixing problem with differential diffusion.

6.4. Results and discussion

We study the model and its implementation presented in Section 6.3 for incorporating the effects of differential diffusion by considering a three-species pure mixing problem in one dimension as described below. The Schmidt numbers of the three species are taken to be $\mathrm{Sc} = \begin{bmatrix} 1 & \frac{1}{4} & \frac{1}{10} \end{bmatrix}$ with reference to a constant viscosity of unity. The governing equations for the mean and the variance of species mass fractions given by Eqs. (96) and (8) respectively reduce to,

$$\frac{\partial\tilde{\phi}_\alpha}{\partial t}=\frac{\partial}{\partial x}\left[\Gamma_{(\alpha)}\frac{\partial\tilde{\phi}_{(\alpha)}}{\partial x}\right]-\frac{\partial}{\partial x}\left[\tilde{\phi}_\alpha\sum_\beta\Gamma_\beta\frac{\partial\tilde{\phi}_\beta}{\partial x}\right], \tag{101}$$

$$\frac{\partial\widetilde{\phi_\alpha'^2}}{\partial t}=-2\Omega_m\widetilde{\phi_\alpha'^2} \tag{102}$$

with the mixing frequency Ω_m being set to unity. Eq. (101) is solved with zero Neumann boundary conditions on each $\tilde{\phi}_\alpha$ and the domain in x-direction is chosen to be sufficiently large such that the value of each $\tilde{\phi}_\alpha$ near the boundary does not change significantly. The mean mass fractions are initialized at time $t=0$ as,

$$\tilde{\phi}_1=\frac{13}{40}[\tanh(20x+8)-\tanh(20x-8)], \tag{103}$$

$$\tilde{\phi}_2=\frac{7}{13}\tilde{\phi}_1, \tag{104}$$

$$\tilde{\phi}_3=1-\tilde{\phi}_1-\tilde{\phi}_2. \tag{105}$$

Given the constraint $\sum_\alpha\phi_\alpha=1$, the realizable region in 3D composition space is a 2D simplex with vertices at $\phi_\beta=\delta_{(\alpha)\beta}$ for each α (δ denotes the Kronecker delta). We initialize the particles in composition space by distributing them on the realizable plane uniformly around a mean composition $\tilde{\boldsymbol{\phi}}$ in a circle of radius ρ_c. As a result, the variance of mass fraction for each species can be shown to be equal to $\rho_c^2/6$. The initial conditions for the mean and mean square of mass fractions are illustrated in Fig. D.19.

Since the solution to Eq. (101) is not known analytically, the results of the PDF calculation are compared to an accurate numerical solution. A numerically accurate solution is obtained by solving Eq. (101) using the Crank–Nicolson method in conjunction with Richardson extrapolation over 512 time steps and on two grids with 512 and 1536 cells for a total time T of $\Omega_m T=3$. For constant Ω_m, the solution to Eq. (102) and the mean square mass fraction are obtained as,

$$\widetilde{\phi_\alpha'^2}(t)=\widetilde{\phi_\alpha'^2}\Big|_{t=0}\exp(-2\Omega_m t), \tag{106}$$

$$\widetilde{\phi_\alpha^2}=\widetilde{\phi_\alpha'^2}+\tilde{\phi}_\alpha^2. \tag{107}$$

Fig. D.20 plots the mean and mean-squared mass fractions at $\Omega_m t=3$. The solid line corresponds to the PDF calculation and the symbols are sampled from the solution obtained from Crank–Nicolson method. Fig. D.21 plots the particles in composition space at the same time on the realizable plane. As can be observed, the implementation ensures that the particles evolve on the realizable plane through the progress of the calculation.

We define mixture fraction based on individual species as,

$$\xi_\alpha=\frac{\phi_\alpha-\phi_{\alpha,0}}{\phi_{\alpha,\infty}-\phi_{\alpha,0}}, \tag{108}$$

where ξ_α is the mixture fraction based on species α, $\phi_{\alpha,0}$ is the mass fraction of species α at $x=0$ and $t=0$, and $\phi_{\alpha,\infty}$ is at $x=\infty$ and $t=0$. In the case of equal Schmidt numbers, the mixture fractions based on individual species is identical and the ratio of any two mass fractions remains constant. In the current test problem with non-unity Schmidt numbers, differential diffusion of individual species yields distinct definitions of mixture fractions. Fig. D.22 compares the estimated mean mixture fractions defined based on the three species taken two at a time. As is evident, differential diffusion effects are significant as the results from the PDF calculations deviate strongly from the line of slope 1.

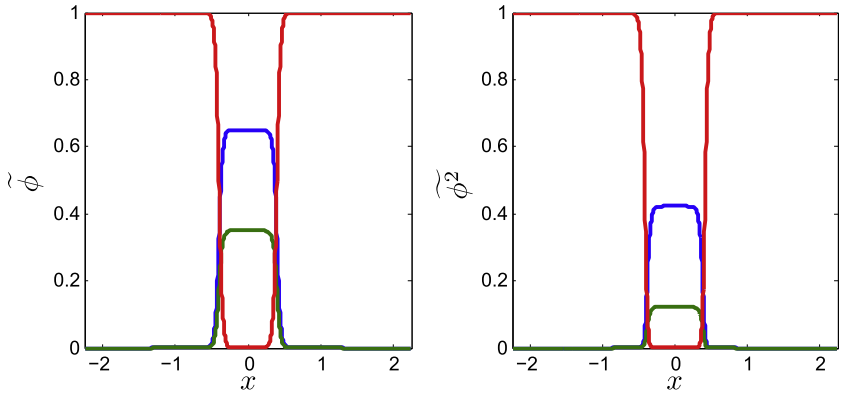

Fig. D.19. Mean and mean square of species mass fractions at $t=0$ for the three species with Schmidt numbers $Sc_1=1$(blue), $Sc_2=\frac{1}{4}$(green) and $Sc_3=\frac{1}{10}$ (red). (For interpretation of the references to color in this figure legend, the reader is referred to the web version of this article.)

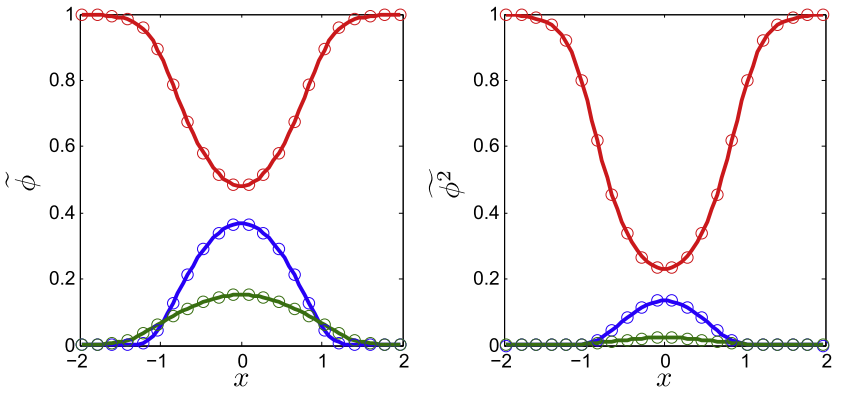

Fig. D.20. Mean and mean square of species mass fraction at $\Omega_m t = 3$ for the three species with Schmidt numbers $\mathrm{Sc}_1 = 1$(blue), $\mathrm{Sc}_2 = \frac{1}{4}$ (green) and $\mathrm{Sc}_3 = \frac{1}{10}$ (red). Solid line corresponds to PDF calculations and the symbols are sampled from the accurate solution obtained using Crank–Nicolson method. (For interpretation of the references to color in this figure legend, the reader is referred to the web version of this article.)

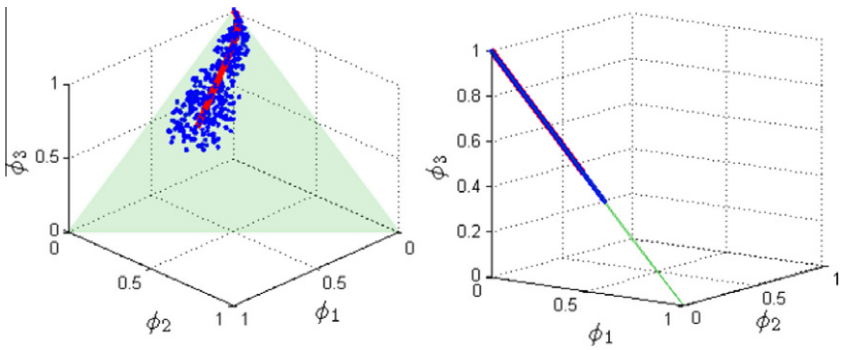

Fig. D.21. Distribution of particle compositions in composition space at $\Omega_m t = 3$. The green plane is the realizable region. The red solid line corresponds to the mean composition field and the blue dots represent particle compositions. The second figure is identical to the first one but is rotated such that the line of sight is along the plane of the realizable region confirming that the numerical implementation preserves realizability. (For interpretation of the references to color in this figure legend, the reader is referred to the web version of this article.)

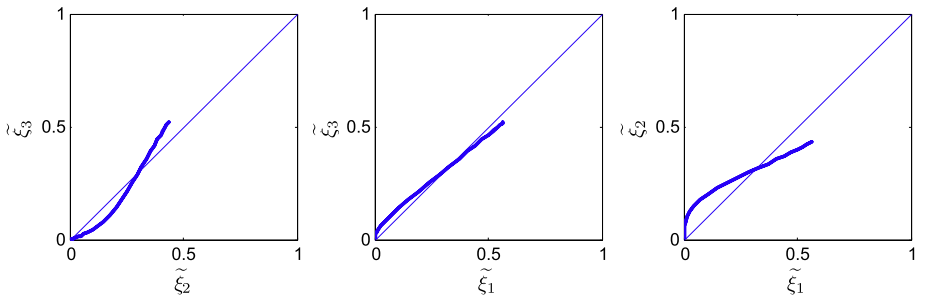

Fig. D.22. Comparison of mean mixture fractions defined based on each species using Eq. (108) at $\Omega_m t = 3$. The thin solid blue line is of slope 1. (For interpretation of the references to color in this figure legend, the reader is referred to the web version of this article.)

In summary, we see that differential diffusion effects can be significant and the current implementation of molecular transport is successful in capturing these effects accurately while ensuring realizability.

7. Conclusions

In this work, we present a model for mixing and molecular transport in the context of PDF methods for turbulent reacting flows based on the work of McDermott and Pope [29]. Mixing is modeled using the IEM model while the effects of molecular transport are directly incorporated as a mean drift term in the scalar evolution equation by Eq. (2). This modeling strategy avoids spurious production of scalar variance even though it neglects the molecular transport of variance in physical space.

In high-Reynolds-number flows, transport in physical space by molecular diffusion can be justified as being negligible. Additionally, this model provides an easy route to incorporating the effects of differential diffusion (Eq. (94)).

We show that the algorithm described for the numerical implementation of the above-mentioned model is second-order accurate in space and time (except for first-order temporal accuracy in the implementation of the convection velocity in the case of differential diffusion). Specifically, three numerical schemes (PIC-PC, PIC-PL and CIC-LS) detailed for the implementation of mixing and molecular transport are evaluated using the Method of Manufactured Solutions (MMS). All the numerical schemes used for the implementation are unconditionally stable and conservative. For a pure mixing problem, the CIC-LS scheme incurs a larger error as compared to the other two schemes whereas there is insignificant difference between the schemes when all processes – transport, mixing and reaction – are treated. For a given accuracy, the CIC-LS scheme is almost thrice as expensive as the other two schemes. Yet, since CIC-LS naturally ensures boundedness of scalars and yields continuous estimated fields, it is preferred over other schemes.

We also present a new variance-reduction methodology by performing implicit smoothing operations. The three-point smoothing scheme is adopted in this work and is shown to satisfy conservation and boundedness criteria. It is also shown to preserve regularity of smooth fields via appropriate handling of empty cells. The accuracy of estimated statistics can be improved significantly for an appropriate choice of the smoothing parameter for very little increase in computational cost. Smoothing can be applied on either the "output" quantities or "feedback" quantities. In this work, a detailed analysis of the root-mean-squared error is performed while smoothing "output" quantities and we infer that the statistical error scales inversely with the total number of particles as $N_{tot}^{-1/2}$ instead of the number of particles per cell $N_{pc}^{-1/2}$ (as is the case with no smoothing). This implies that with smoothing of "feedback" quantities, the bias error scales inversely with the total number of particles, N_{tot}^{-1} in the domain instead of the number of particles per cell N_{pc}^{-1}. Moreover, we present a model for the root-mean-squared error obtained after smoothing of the "output" quantities that is successful in explaining the behavior portrayed by the data obtained from PDF calculations. One of the primary predictions of this model is that the root-mean-squared error after smoothing depends weakly on N_{tot} as $N_{tot}^{-2/7}$ in 3D. It should be noted that this analysis is corroborated against numerical calculations performed based on the MMS methodology.

Finally, we present a model (and a numerical implementation) that accounts for differential diffusion effects in the scalar evolution equation. We show that this model and the corresponding numerical algorithm described in this work satisfy conservation and realizability constraints but the asymmetry of the splitting scheme reduces the temporal accuracy to first-order in the presence of differential diffusion. The model and the algorithm are studied in one dimension considering pure mixing of three non-unity Schmidt number scalars. It is shown that the effects of differential diffusion can be significant and the current implementation is successful in capturing these effects accurately while ensuring realizability.

Acknowledgments

We would like to thank Steve R. Lantz for useful pointers through this work. This research is supported by the Department of Energy under Grant DE-FG02-90ER14128. This research was conducted using the resources of the Cornell University Center for Advanced Computing, which receives funding from Cornell University, New York State, the National Science Foundation, and other leading public agencies, foundations, and corporations.

Appendix A. Numerical solution of the heat conduction equation

The numerical solution to the heat conduction equation is required both in the estimation of mean shifts due to molecular transport (Section 3) and in performing the smoothing operation (Section 3.4). This appendix details the methodology used in obtaining the numerical solution of the 3D variable-property heat conduction equation using the Crank–Nicolson Finite Volume (CN-FV) scheme, and it is organized as follows. First, we consider the numerical solution to the 3D variable-property heat conduction equation for a single species. Next, we present a description of the Locally One Dimensional (LOD) scheme (a variant of the Alternating Direction Implicit (ADI) scheme) used to simplify the numerical solution of the 3D variable-property heat conduction equation. Finally, we conclude this appendix by extending this algorithm to incorporate the general case of multiple species with different diffusivities.

A.1. Crank–Nicolson finite volume scheme

The primary object of discussion in this section is the numerical solution of the 3D variable-property heat conduction equation:

$$\frac{\partial \rho\tilde{\phi}}{\partial t} = \frac{\partial}{\partial x_j}\left(\rho\Gamma\frac{\partial\tilde{\phi}}{\partial x_j}\right), \tag{A.1}$$

where ρ is the density, $\tilde{\phi}$ is the conserved scalar being diffused (the scalar mean, for instance) and Γ is its conductivity or diffusivity.

The formulation of the finite-volume equation here in Appendix A.1 and their solution in Appendix (A.2) is standard. It is necessary, however, to develop the equations involved in order to establish the conservation and boundedness properties of operations involved.

Consider a closed domain of volume L^3 in a Cartesian coordinate system. Consider this volume to be discretized into $N_{\text{cell}} = N_x N_y N_z$ sub-volumes (or cells) where each coordinate direction x, y and z is discretized into N_x, N_y and N_z 1D-cells respectively. Let $\mathbf{x}_p = (x_i, y_j, z_k)$ for $i = 1,2,\ldots,N_x,\ j = 1,2,\ldots,N_y$ and $k = 1,2,\ldots,N_z$ denote the center of the pth cell where a lexicographical reordering is used to obtain the index p as $p = (k-1)N_xN_y + (j-1)N_x + i$. Further, let $\bar{x}_i, \bar{y}_j$ and $\bar{z}_k$ denote the vertices in each direction with $i = 0,1,2,\ldots,N_x$, $j = 0,1,2,\ldots,N_y$ and $k = 0,1,2,\ldots,N_z$. The cell width in each direction is obtained as,

$$\Delta x_i = \bar{x}_i - \bar{x}_{i-1}, \tag{A.2}$$

$$\Delta y_j = \bar{y}_j - \bar{y}_{j-1}, \tag{A.3}$$

$$\Delta z_k = \bar{z}_k - \bar{z}_{k-1}, \tag{A.4}$$

for $i = 1,2,\ldots,N_x,\ j = 1,2,\ldots,N_y$ and $k = 1,2,\ldots,N_z$. For simplicity of illustration, Fig. D.23 presents a pictorial representation of the notation described above in a 2D Cartesian system for $N_x = 4$ and $N_y = 3$.

Consider obtaining a numerical solution $\tilde{\phi}_p$ defined at cell-centers $\mathbf{x}_p$ to the 3D heat conduction equation given by Eq. (A.1) using the Crank–Nicolson Finite Volume scheme by advancing $\tilde{\phi}$ across a time step Δt from a time level $t_n = n\Delta t$ to $t_{n+1} = (n+1)\Delta t$. The coefficients are frozen at a time level of $n+\frac{1}{2}$ and any quantity Q is obtained as,

$$Q^{n+\frac{1}{2}} = \frac{Q^n + Q^{n+1}}{2}, \tag{A.5}$$

$$Q_{i-\frac{1}{2},j,k} = \frac{Q_{i,j,k}\Delta x_{i-1} + Q_{i-1,j,k}\Delta x_i}{\Delta x_i + \Delta x_{i-1}}, \tag{A.6}$$

$$Q_{i,j-\frac{1}{2},k} = \frac{Q_{i,j,k}\Delta y_{j-1} + Q_{i,j-1,k}\Delta y_j}{\Delta y_j + \Delta y_{j-1}}, \tag{A.7}$$

$$Q_{i,j,k-\frac{1}{2}} = \frac{Q_{i,j,k}\Delta z_{k-1} + Q_{i,j,k-1}\Delta z_k}{\Delta z_k + \Delta z_{k-1}}. \tag{A.8}$$

Let W be a diagonal matrix with $W_{pp} = m_p = m_{i,j,k}$, where m_p (defined below in Appendix C) is the mass of the cell centered at $\mathbf{x}_p$ and let M be a banded matrix with bandwidth of at most $2N_xN_y$ with off-diagonal entries:

$$M_{p,p-1} = m_{i-\frac{1}{2},j,k}\Gamma^{n+\frac{1}{2}}_{i-\frac{1}{2},j,k}/\Delta x^2_{i-\frac{1}{2}}, \tag{A.9}$$

$$M_{p,p+1} = m_{i+\frac{1}{2},j,k}\Gamma^{n+\frac{1}{2}}_{i+\frac{1}{2},j,k}/\Delta x^2_{i+\frac{1}{2}}, \tag{A.10}$$

$$M_{p,p-N_x} = m_{i,j-\frac{1}{2},k}\Gamma^{n+\frac{1}{2}}_{i,j-\frac{1}{2},k}/\Delta y^2_{j-\frac{1}{2}}, \tag{A.11}$$

$$M_{p,p+N_x} = m_{i,j+\frac{1}{2},k}\Gamma^{n+\frac{1}{2}}_{i,j+\frac{1}{2},k}/\Delta y^2_{j+\frac{1}{2}}, \tag{A.12}$$

$$M_{p,p-N_xN_y} = m_{i,j,k-\frac{1}{2}}\Gamma^{n+\frac{1}{2}}_{i,j,k-\frac{1}{2}}/\Delta z^2_{k-\frac{1}{2}}, \tag{A.13}$$

$$M_{p,p+N_xN_y} = m_{i,j,k+\frac{1}{2}}\Gamma^{n+\frac{1}{2}}_{i,j,k+\frac{1}{2}}/\Delta z^2_{k+\frac{1}{2}}, \tag{A.14}$$

where $2\Delta x_{i-\frac{1}{2}} = \Delta x_i + \Delta x_{i-1}$. The definitions for $\Delta y_{j-\frac{1}{2}}$ and $\Delta z_{k-\frac{1}{2}}$ follow similarly and by construction, $\sum_q M_{pq} = 0$.

Given $\tilde{\phi}^n_p$, W, and M, the change in solution $\Delta\tilde{\phi}^h$ to the heat conduction equation given by Eq. (A.1) over a time-step Δt can be written in matrix form as,

$$W\Delta\tilde{\phi}^{h,n+\frac{1}{2}} = \Delta t M\tilde{\phi}^{n+\frac{1}{2}}, \tag{A.15}$$

where $\Delta\tilde{\phi}^{h,n+1/2} = \tilde{\phi}^{n+1} - \tilde{\phi}^n \equiv \Delta\tilde{\phi}^{n+\frac{1}{2}}$. Or equivalently, we can re-write Eq. (A.15) in index notation as,

$$m_{(p)}\Delta\tilde{\phi}^{n+\frac{1}{2}}_p = \Delta t M_{pq}\tilde{\phi}^{n+\frac{1}{2}}_q, \tag{A.16}$$

where indices in parentheses are not included in the summation convention. By the definition of M,

$$\sum_p m_p\Delta\tilde{\phi}^{n+\frac{1}{2}}_p = \Delta t\underbrace{\sum_p M_{pq}}_{0}\tilde{\phi}^{n+\frac{1}{2}}_q = 0. \tag{A.17}$$

Further Eq. (A.15) can be re-arranged in-terms of known quantities to give,

$$\left[W - \frac{\Delta t}{2}M\right]\tilde{\phi}^{n+1} = \left[W + \frac{\Delta t}{2}M\right]\tilde{\phi}^n. \tag{A.18}$$

The CN-FV scheme detailed above is second-order accurate in space and time and is unconditionally stable.

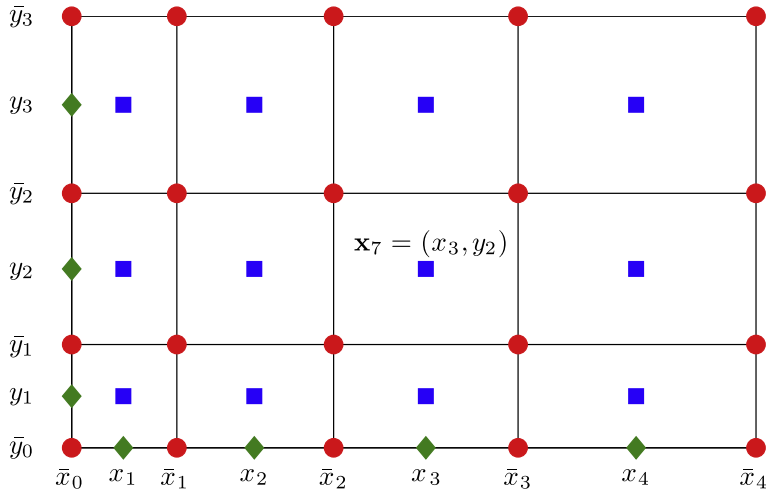

Fig. D.23. Illustration of a 2D grid with $N_x = 4$ and $N_y = 3$. The physical domain considered is of size L^2 with $\bar{x}_0 = 0,\ \bar{x}_{N_x} = L,\ \bar{y}_0 = 0,\ \bar{y}_{N_y} = L$. The vertices $\bar{x}$ and $\bar{y}$ are denoted using (circles); the cell centers x and y (in 1D) are denoted using (diamonds); and the cell-center of the pth cell $\mathbf{x}_p$ is denoted using (squares). To illustrate the lexicographical re-ordering used, $\mathbf{x}_7$ is denoted on the plot.

A.2. Locally One Dimensional ADI scheme

As mentioned in the previous section, the bandwidth of the system of equations considered (Eq. (A.18)) is at most $2N_xN_y$ and we approximate it as the product of tri-diagonal matrices (and permutations) by incorporating Alternating Direction Implicit (ADI) methods. There are many variants of the ADI scheme but the Locally One Dimensional (LOD) scheme is of interest here and is described below. The LOD scheme has the additional advantage of resulting in a numerical solution procedure equivalent to solving a 1D heat conduction equation successively in each direction.

Consider X to be a tri-diagonal square matrix of size N_x defined by:

$$\begin{aligned} X_{i,i-1} &= \frac{m_{i-\frac{1}{2},j,k}\Gamma^{n+\frac{1}{2}}_{i-\frac{1}{2},j,k}}{\Delta x^2_{i-\frac{1}{2}}}, \\ X_{i,i+1} &= \frac{m_{i+\frac{1}{2},j,k}\Gamma^{n+\frac{1}{2}}_{i+\frac{1}{2},j,k}}{\Delta x^2_{i+\frac{1}{2}}}, \\ X_{i,i} &= -X_{i,i-1} - X_{i,i+1} \end{aligned} \tag{A.19}$$

with $i = 1, 2, \ldots, N_x$ for every j and k. Similarly, Y and Z of sizes N_y and N_z respectively are defined as:

$$\begin{aligned} Y_{j,j-1} &= \frac{m_{i,j-\frac{1}{2},k}\Gamma^{n+\frac{1}{2}}_{ij-\frac{1}{2},k}}{\Delta y^2_{j-\frac{1}{2}}}, \\ Y_{j,j+1} &= \frac{m_{ij+\frac{1}{2},k}\Gamma^{n+\frac{1}{2}}_{ij+\frac{1}{2},k}}{\Delta y^2_{j+\frac{1}{2}}}, \\ Y_{j,j} &= -Y_{j,j-1} - Y_{j,j+1}, \end{aligned} \tag{A.20}$$

and

$$\begin{aligned} Z_{k,k-1} &= \frac{m_{i,j,k-\frac{1}{2}}\Gamma^{n+\frac{1}{2}}_{i,j,k-\frac{1}{2}}}{\Delta z^2_{k-\frac{1}{2}}}, \\ Z_{k,k+1} &= \frac{m_{i,j,k+\frac{1}{2}}\Gamma^{n+\frac{1}{2}}_{i,j,k+\frac{1}{2}}}{\Delta z^2_{k+\frac{1}{2}}}, \\ Z_{k,k} &= -Z_{k,k-1} - Z_{k,k+1} \end{aligned} \tag{A.21}$$

with $j = 1, 2, \ldots, N_y$ and $k = 1, 2, \ldots, N_z$.

We approximate the numerical solution obtained by solving Eq. (A.18) by solving each of the following three sub-steps given by the LOD scheme successively in each direction:

$$\left[W-\frac{\Delta t}{2}X\right]\tilde{\phi}^{s1}=\left[W+\frac{\Delta t}{2}X\right]\tilde{\phi}^{n}, \tag{A.22}$$

$$\left[W-\frac{\Delta t}{2}Y\right]\tilde{\phi}^{s2}=\left[W+\frac{\Delta t}{2}Y\right]\tilde{\phi}^{s1}, \tag{A.23}$$

$$\left[W-\frac{\Delta t}{2}Z\right]\tilde{\phi}^{n+1}=\left[W+\frac{\Delta t}{2}Z\right]\tilde{\phi}^{s2}. \tag{A.24}$$

Each sub-step of the LOD scheme given corresponding to Eqs. (A.22)–(A.24) is equivalent to solving the one-dimensional heat conduction equation successively and can be numerically solved using the Tri-Diagonal Matrix Algorithm (TDMA) in $\mathcal{O}(N)$ operations. For periodic problems, the Sherman–Morrison–Woodbury formula is used. It should be noted that the transition between the sub-steps occurs with appropriate permutations on $\tilde{\phi}$. Additionally, note that the LOD scheme is unconditionally stable and conservative.

To summarize, thus far we present a methodology to estimate the mean drifts for the special case of either a single species or multiple species with the same molecular diffusivity. The following section describes an algorithm to calculate the mean drifts in the presence of differential diffusion.

A.3. Differential diffusion

In this section, we present a numerical implementation of the variable-property heat conduction equation in the presence of differential diffusion of multiple species mass fractions. The algorithm is presented in one-dimension but is easily extended to multiple dimensions without any violation of the properties of the scheme.

Consider a set of n_s transport equations for species mass fractions $\tilde{\phi}_\alpha$ for $\alpha=1,2,\ldots,n_s$ in the x-direction:

$$\frac{\partial\rho\tilde{\phi}_\alpha}{\partial t}+\frac{\partial\rho V_{(\alpha)}\tilde{\phi}_\alpha}{\partial x}=0, \tag{A.25}$$

where V_α is the diffusion velocity in the x-direction. Note that indices in parentheses are excluded from the summation convention. We consider modeling diffusion velocities using Fick's law as

$$(V_{(\alpha)}+V_c)\tilde{\phi}_\alpha=-\Gamma_{(\alpha)}\frac{\partial\tilde{\phi}_\alpha}{\partial x}, \tag{A.26}$$

where Γ_α is the mixture-averaged diffusivity of species α and the correction velocity V_c is given by

$$V_c=-\sum_\alpha\Gamma_\alpha\frac{\partial\tilde{\phi}_\alpha}{\partial x}. \tag{A.27}$$

Given Eqs. (A.26) and (A.27), Eq. (A.25) can be written as,

$$\frac{\partial\rho\tilde{\phi}_\alpha}{\partial t}=\frac{\partial}{\partial x}\left(\rho\Gamma_{(\alpha)}\frac{\partial\tilde{\phi}_\alpha}{\partial x}\right)-\frac{\partial}{\partial x}\left(\rho\tilde{\phi}_\alpha\sum_\beta\Gamma_\beta\frac{\partial\tilde{\phi}_\beta}{\partial x}\right). \tag{A.28}$$

The numerical solution to Eq. (A.28) is obtained in two steps. First, given $\tilde{\phi}_\alpha^n$, the heat conduction equation without the correction term:

$$\frac{\partial\rho\tilde{\phi}_\alpha}{\partial t}=\frac{\partial}{\partial x}\left(\rho\Gamma_{(\alpha)}\frac{\partial\tilde{\phi}_\alpha}{\partial x}\right) \tag{A.29}$$

is solved to obtain the increment $\Delta\tilde{\phi}_\alpha^{h,n+\frac{1}{2}}=\tilde{\phi}_\alpha^{h,n+1}-\tilde{\phi}_\alpha^n$ over a time-step Δt using the CN-FV scheme as

$$W\Delta\tilde{\phi}_\alpha^{h,n+\frac{1}{2}}=\Delta tX_{(\alpha)}\tilde{\phi}_\alpha^{h,n+\frac{1}{2}} \tag{A.30}$$

for each α with $2\tilde{\phi}_\alpha^{h,n+\frac{1}{2}}=\tilde{\phi}_\alpha^{h,n+1}+\tilde{\phi}_\alpha^n$ where X_α is given by Eq. (A.19) with Γ replaced by Γ_α. This step is implicit and second-order accurate in space and time. Note that summing Eq. (A.30) over all rows yields,

$$\sum_p W_{pp}\Delta\tilde{\phi}_{\alpha,p}^{h,n+\frac{1}{2}}=\Delta t\underbrace{\sum_p X_{\alpha;pq}}_{=0}\tilde{\phi}_{\alpha,q}^{h,n+\frac{1}{2}}=0. \tag{A.31}$$

Eq. (A.30) can be represented in terms of known quantities as:

$$\left(W-\frac{\Delta t}{2}X_\alpha\right)\tilde{\phi}_\alpha^{h,n+\frac{1}{2}}=\left(W+\frac{\Delta t}{2}X_\alpha\right)\tilde{\phi}_\alpha^n. \tag{A.32}$$

Secondly, given $\tilde{\phi}_\alpha^{h,n+\frac{1}{2}}$, we define V for each $j = 1, 2, \ldots, N_y$ and $k = 1, 2, \ldots, N_z$ as:

$$V_{i+\frac{1}{2}} = \sum_\alpha X_{\alpha;i,i+1}\left(\tilde{\phi}^{h,n+\frac{1}{2}}_{\alpha;i+1,j,k} - \tilde{\phi}^{h,n+\frac{1}{2}}_{\alpha;i,j,k}\right). \tag{A.33}$$

Using $\tilde{\phi}_\alpha^n$ and V, we solve

$$\frac{\partial \rho\tilde{\phi}_\alpha}{\partial t} = \frac{\partial(\rho\tilde{\phi}_\alpha V_c)}{\partial x} \tag{A.34}$$

over the time-step Δt explicitly to obtain the correction $\Delta\tilde{\phi}_\alpha^{c,n+\frac{1}{2}}$ as,

$$W\Delta\tilde{\phi}_\alpha^{c,n+\frac{1}{2}} = \Delta t N\tilde{\phi}_\alpha^n, \tag{A.35}$$

where N is a tri-diagonal matrix defined as:

$$N_{i-1,i} = \frac{V_{i-\frac{1}{2}}}{2}, \tag{A.36}$$

$$N_{i+1,i} = -\frac{V_{i+\frac{1}{2}}}{2}. \tag{A.37}$$

Note that by construction, $\sum_i N_{ij} = 0$. This implies that the summation over all rows of Eq. (A.35) yields zero.

Finally, the increment $\Delta\tilde{\phi}_\alpha^{n+\frac{1}{2}}$ is obtained as,

$$\Delta\tilde{\phi}_\alpha^{n+\frac{1}{2}} = \Delta\tilde{\phi}_\alpha^{h,n+\frac{1}{2}} - \Delta\tilde{\phi}_\alpha^{c,n+\frac{1}{2}} \tag{A.38}$$

based on which, the following observations can be made:

1. Summing Eq. (A.38) over all species α yields zero *i.e.*,

$$\sum_\alpha \Delta\tilde{\phi}_\alpha^{n+\frac{1}{2}} = 0. \tag{A.39}$$

2. Summing Eq. (A.38) weighted by W over all rows sums to zero as well,

$$\sum_p W_{pp}\Delta\tilde{\phi}_{\alpha,p}^{n+\frac{1}{2}} = 0, \tag{A.40}$$

since summing over all rows of both N and X_α is zero.

In summary, this section presents an implementation methodology that accounts for differential diffusion effects in one-dimension. In higher dimensions, the LOD scheme is used and the correction $\Delta\tilde{\phi}_\alpha^c$ is applied at each sub-step of the LOD scheme.

Appendix B. Smoothing

Many families of smoothing schemes can be formulated originating from the generalized variable-property heat conduction equation by implementing various numerical schemes such as the implicit Euler scheme. In Appendix B.1, a brief mention is made about the various smoothing schemes derived from the heat-conduction equation with specific reference to the three-point implicit smoothing methodology. Following this, Appendix B.2 presents a detailed analysis (in wave number space) of the smearing error incurred upon smoothing and the corresponding variance reduction achieved for the three-point implicit smoothing scheme.

B.1. Explicit smoothing vs. implicit smoothing

In this section of the appendix on smoothing, we present a class of implicit–explicit smoothing schemes derived from the variable-property heat conduction equation using the Crank–Nicolson scheme. The three-point implicit smoothing scheme is of particular interest in this work.

Let us consider formulating a smoothing scheme starting with the variable-property heat equation in 1D given by Eq. (A.29). As described in Appendix A.1, the discrete representation of the heat equation using the CN-FV scheme yields Eq. (A.32), which when adapted to smoothing becomes,

$$(W + A)g = (W + B)f. \tag{B.1}$$

The noisy input field f and the smoothed output field g are both weighted by the diagonal matrix W. The matrix A performs the implicit smoothing operation and B corresponds to the explicit smoothing operation. Each specification for the matrices A and B, that satisfies the set of properties mentioned in Section 3.4.2, yields a family of smoothing schemes. In this work, we

are interested in a smoothing scheme with a three-point stencil that yields A and B in tri-diagonal form. Computational algorithms such as the tri-diagonal matrix solvers can be used to solve the resulting linear system relatively inexpensively.

The three-point scheme is parametrized by two parameters: α_s parametrizes the smoothing matrix A, and β_s parametrizes the smoothing matrix B. The following specification for A and B,

$$A_{j,j-1} = -\alpha_s, \quad A_{j,j+1} = -\alpha_s, \quad A_{j,j} = 2\alpha_s, \tag{B.2}$$

$$B_{j,j-1} = \beta_s, \quad B_{j,j+1} = \beta_s, \quad B_{j,j} = -2\beta_s \tag{B.3}$$

satisfies the properties listed in Section 3.4.2 for non-negative α_s and β_s and this is identical to the specification introduced in Eqs. (12) and (13). The process of smoothing not only achieves a reduction in variance *i.e.*, $\mathrm{var}(g) \leqslant \mathrm{var}(f)$ but also incurs a spatial smearing error. A simple analysis (not shown here) in wave number space shows that for a given reduction in variance, minimal smearing error is incurred for $\beta_s = 0$. Henceforth, we consider only the three-point implicit smoothing scheme given by Eq. (32) repeated here for coherence:

$$(W + A)g = Wf.$$

It should be noted that in Eq. (32), f enters solely as Wf. Consequently, if $w_i = 0$ then $(Wf)_i = 0$ regardless of the value of f_i. In a situation where the ith cell is devoid of particles and is empty, $w_i = 0$ and therefore g_i contains no contribution from the undefined f_i.

B.2. Smearing error in smoothing

The operation of smoothing has a twofold effect on the smoothed fields g in comparison to the fields input for smoothing f: variance reduction and spatial smearing. Here, we present an analysis in wave number space to estimate the smearing error incurred given the three-point implicit smoothing scheme parametrized by α_s. This analysis is later used towards the end of this section to model the smearing error due to smoothing of "output" quantities in a PDF calculation.

Consider a periodic function $H(x)$, in one dimension with period L, to be specified. We sample $H(x)$ at N equally spaced points x_j for $j = 0, 1, \ldots, N-1$ to get

$$H_j \equiv H(x_j) \tag{B.4}$$

and define $\Delta x = L/N$ such that $x_j = j\Delta x$. The discrete inverse Fourier transform of H_j is obtained as

$$H_j = \sum_{k=1-\frac{N}{2}}^{\frac{N}{2}} \widehat{H}_k e^{i\kappa_k x_j}, \tag{B.5}$$

where $\kappa_k = 2\pi k/L$ and

$$\widehat{H}_k = a_{H,k} + i b_{H,k}. \tag{B.6}$$

Since H_j is real, $\widehat{H}_k$ satisfies conjugate symmetry resulting in $a_{H,k} = a_{H,-k}$ and $b_{H,k} = -b_{H,-k}$.

Next, consider $f(x)$ to be an estimate of $H(x)$ and $f_j \equiv f(x_j)$ such that

$$f_j = H_j + \mu_j \tag{B.7}$$

for some deterministic error $\mu_j \equiv \mu(x_j)$. As in Eq. (B.5), the discrete inverse Fourier transforms of μ_j and f_j are obtained as,

$$\mu_j = \sum_{k=1-\frac{N}{2}}^{\frac{N}{2}} \hat{\mu}_k e^{i\kappa_k x_j} \tag{B.8}$$

and

$$\hat{f}_k = \widehat{H}_k + \hat{\mu}_k, \tag{B.9}$$

respectively with

$$\hat{\mu}_k = a_{\mu,k} + i b_{\mu,k}. \tag{B.10}$$

As with H_j, since μ_j is real, conjugate symmetry implies that $a_{\mu,k} = a_{\mu,-k}$ and $b_{\mu,k} = -b_{\mu,-k}$.

We perform a three-point implicit smoothing operation on f_j using Eq. (50) to obtain g_j as

$$g_i = C_{ij} f_j, \tag{B.11}$$

the Fourier transform of which results in

$$\hat{g}_k = \widehat{C}_k \hat{f}_k, \tag{B.12}$$

where $\hat{g}_k$ is the Fourier transform of g_j and $\widehat{C}_k$ is that of C_{ij}. For A defined by Eq. (B.2), it can be shown that

$$\widehat{C}_k = \frac{1}{1 + 2\alpha_s E_k}, \tag{B.13}$$

where

$$E_k = 1 - \cos(\kappa_k \Delta x). \tag{B.14}$$

Note that given Eqs. (B.13) and (B.14), $\widehat{C}$ has zero phase.

Let us define the Fourier transform $\widehat{S}_k$ of the smearing error $S_j \equiv S(x_j) = g_j - H_j$ as

$$\widehat{S}_k = \hat{g}_k - \widehat{H}_k, \tag{B.15}$$

$$= (\widehat{C}_k - 1)\widehat{H}_k + \widehat{C}_k \hat{\mu}_k, \tag{B.16}$$

where the last line is obtained by substituting Eqs. (B.9) and (B.12) in Eq. (B.15). Now, consider $\mathcal{S}$ to be the global estimate of the smearing error S_j given by

$$\begin{aligned} \mathcal{S}^2 &= \sum_{j=0}^{N-1} S_j^2, \\ &= \sum_{k=1-\frac{N}{2}}^{\frac{N}{2}} \widehat{S}_k \widehat{S}_k^*, \\ &= \sum_{k=1-\frac{N}{2}}^{\frac{N}{2}} |\widehat{S}_k|^2, \end{aligned} \tag{B.17}$$

where $\widehat{S}_k^*$ is the complex conjugate of $\widehat{S}_k$. The second line in Eq. (B.17) follows from Parseval's theorem and the last line is obtained by using $|\widehat{S}_k|^2 = \widehat{S}_k \widehat{S}_k^*$. Since $|\widehat{S}_k|^2 = |\widehat{S}_{-k}|^2$, using Eqs. (B.6), (B.10), (B.13) and (B.16) in Eq. (B.17), we obtain the global estimate of the smearing error to be

$$\mathcal{S}^2 = |\hat{\mu}_0|^2 + 2\sum_{k=1}^{\frac{N}{2}} \left(\frac{2\alpha_s E_k}{1 + 2\alpha_s E_k}\right)^2 |\widehat{H}_k|^2 + 2\sum_{k=1}^{\frac{N}{2}} \left(\frac{1}{1 + 2\alpha_s E_k}\right)^2 |\hat{\mu}_k|^2 - 2\sum_{k=1}^{\frac{N}{2}} \frac{4\alpha_s E_k}{(1 + 2\alpha_s E_k)^2} (a_{H,k} a_{\mu,k} + b_{H,k} b_{\mu,k}). \tag{B.18}$$

Note that $A_\mu^2 \equiv |\hat{\mu}_k|^2 = a_{\mu,k}^2 + b_{\mu,k}^2$. The definition for $A_H^2 \equiv |\widehat{H}_k|^2$ follows.

Eq. (B.18) can be used to obtain the global estimate of the smearing error due to smoothing f_j implicitly with parameter α_s when $\widehat{H}$ and $\hat{\mu}$ are known. Typically, in a PDF calculation, neither of these are known *a priori* and in the following paragraphs, we present an approximate model for $\mathcal{S}$ under the assumption that H_j and μ_j consist of a single mode each at wave-numbers κ_H and κ_μ, respectively.

Given H_j, κ_H and A_H are known. Consider μ_j to arise primarily due to spatial truncation errors (second-order accurate in this work). Then, the following can be inferred:

$$E_{\kappa_H} \sim \Delta x^2, \tag{B.19}$$

$$A_\mu \sim \Delta x^2, \tag{B.20}$$

$$\kappa_\mu \sim \frac{1}{\Delta x}, \tag{B.21}$$

$$E_{\kappa_\mu} \sim \text{constant}. \tag{B.22}$$

We present models for $\mathcal{S}^2$ for the following two cases:

1. When $\kappa_H \neq \kappa_\mu$, the global estimate of the smearing error $\mathcal{S}$ given by Eq. (B.18) can be simplified to get

$$\mathcal{S}^2 = \left(\frac{c_1 \alpha_s \Delta x^2}{1 + c_2 \alpha_s \Delta x^2}\right)^2 + \left(\frac{c_3 \Delta x^2}{1 + c_4 \alpha_s}\right)^2 \tag{B.23}$$

   for some c_i.
2. When $\kappa_H = \kappa_\mu, \mathcal{S}$ in Eq. (B.18) is simplified to get

$$\mathcal{S}^2 = \left(\frac{c_1 \Delta x^2 - c_2 \alpha_s \Delta x^2}{1 + c_3 \alpha_s \Delta x^2}\right)^2 + \left(\frac{c_4 \Delta x^2 - c_5 \alpha_s \Delta x^2}{1 + c_3 \alpha_s \Delta x^2}\right)^2 \tag{B.24}$$

   for some other c_i.

It should be noted however, that the preceding analysis yields an approximate model for $\mathcal{S}$ since only one or two modes were considered to obtain Eqs. (B.24) and (B.23).

B.3. Variance reduction in smoothing

We briefly present an expression for the reduction in variance achieved due to smoothing in this section of Appendix B. Let V denote the ratio $\mathrm{var}(f)/\mathrm{var}(g)$. An exact expression for V is easily obtained in 1D using Eq. (B.12) as

$$V^{-1} = \frac{1}{\kappa}\int_0^{\kappa} \widehat{C}(\hat{\kappa})^2 d\hat{\kappa}, \tag{B.25}$$

$$= \frac{1+2\alpha_s}{(1+4\alpha_s)^{3/2}}. \tag{B.26}$$

Since LOD is used to perform smoothing in higher dimensions, it follows that in a D-dimensional space the variance reduction is obtained as,

$$V = \left[\frac{(1+4\alpha_s)^{3/2}}{1+2\alpha_s}\right]^D. \tag{B.27}$$

In summary, Appendix B presents a brief introduction to the various explicit and implicit smoothing methodologies followed by an analysis of the smearing error due to smoothing in wave-number space, concluding with approximate models for the smearing error and an exact expression for the variance reduction.

Appendix C. Properties of various schemes

Consider $\phi^{*,n}_{\alpha,p}$ to represent the mass fraction of species α for a general particle p at a time level n. All particle properties are denoted with a superscript '$*$'. Any numerical scheme presented for the implementation of mixing must satisfy the following three criteria:

1. Detailed conservation at the particle level given by

$$\sum_p m_p \phi^{*,n+1}_{\alpha,p} = \sum_p m_p \phi^{*,n}_{\alpha,p}, \tag{C.1}$$

where m_p is the mass of the particle p.

2. Boundedness of species mass fractions which requires that mass fractions be positive at all times:

$$\phi_\alpha \geqslant 0. \tag{C.2}$$

3. Normalization constraint on species mass fractions:

$$\sum_\alpha \phi_\alpha = 1. \tag{C.3}$$

A set of mass fractions is realizable if both the normalization condition and boundedness is satisfied. Boundedness can be imposed by fixing a lower limit on the mixing frequency [29] while considering the implementation of IEM mixing and molecular transport together. Therefore, this section is divided into two parts: the first analyzes each of the schemes *viz.*, PIC-PC, PIC-PL and CIC-LS for realizability and the second part concentrates on the conservation properties of each scheme.

C.1. Realizability

Realizability is satisfied if both the boundedness and normalization conditions are satisfied. Consider Eq. (98) repeated here for convenience,

$$\phi^{*,n+1}_{\alpha,p} = \phi^{*,n}_{\alpha,p} + c_p^{*,n+\frac{1}{2}}\left(\tilde{\phi}^{*,n}_{\alpha,p} - \phi^{*,n}_{\alpha,p}\right) + \Delta\tilde{\phi}^{*,n+\frac{1}{2}}_{\alpha,p},$$

where $\Delta\tilde{\phi}_p^{*,n+\frac{1}{2}}$ is given by Eq. (A.38). McDermott and Pope [29] show that boundedness can be achieved by imposing a lower limit on the mixing frequency as:

$$c_p^{*,n+\frac{1}{2}} \geqslant c_{\min}^{n+\frac{1}{2}} \equiv \max_{p,\alpha}\left[\frac{\Delta\tilde{\phi}^{*,n+1/2}_{\alpha,p}}{\phi^n_{\max} - \tilde{\phi}^{*,n}_{\alpha,p}}, \frac{\Delta\tilde{\phi}^{*,n+1/2}_{\alpha,p}}{\phi^n_{\min} - \tilde{\phi}^{*,n}_{\alpha,p}}\right], \tag{C.4}$$

where $\phi^n_{\min} \leqslant \phi^{*,n}_{\alpha,p} \leqslant \phi^n_{\max}$. Given that boundedness is satisfied by imposing a lower limit on the mixing frequency, realizability is achieved by satisfying the normalization condition given by Eq. (C.3).

We show that, given that $\phi^{*,n}_{\alpha,p}$ satisfies the normalization condition, a necessary and sufficient condition for $\phi^{*,n+1}_{\alpha,p}$ to satisfy the normalization condition is that $\tilde{\phi}^{*,n}_{\alpha,p}$ also satisfy the normalization condition. Consider summing Eq. (98) over all species:

$$\sum_{\alpha}\phi^{*,n+1}_{\alpha,p} = \underbrace{\sum\nolimits_{\alpha}\phi^{*,n}_{\alpha,p}}_{1} + c^{*,\frac{1}{2}}_{p}\left(\sum_{\alpha}\tilde{\phi}^{*,n}_{\alpha,p} - \underbrace{\sum\nolimits_{\alpha}\phi^{*,n}_{\alpha,p}}_{1}\right) + \underbrace{\sum\nolimits_{\alpha}\Delta\tilde{\phi}^{*,\frac{1}{2}}_{\alpha,p}}_{0}.$$

where the last term stems from Eq. (A.39) since interpolation preserves the normalization condition. As elaborated in Section 3.3, $\tilde{\phi}^{*,n}_{\alpha,p}$ (or $\Delta\tilde{\phi}^{*,n}_{\alpha,p}$) is obtained by interpolating $\tilde{\phi}^{n}_{\alpha,j}$ (or $\Delta\tilde{\phi}^{n}_{\alpha,j}$) to particle locations using one of the three interpolation schemes: PC, LS or PL.

Note that $\tilde{\phi}^{n}_{\alpha,j}$ is the smoothed estimate of the mean of species α obtained by smoothing $\hat{\phi}^{n}_{\alpha,j}$ using the implicit smoothing scheme represented by Eq. (32). If $f_j \equiv \sum_\alpha \hat{\phi}_{\alpha,j} = 1$, then $g_j \equiv \sum_\alpha \tilde{\phi}_{\alpha,j} = 1$ because of boundedness (shown in Section 3.4.2), *i.e.*, $\min_j f_j = 1 \leqslant g_j \leqslant \max_j f_j = 1$. Therefore, smoothing preserves the normalization condition.

Finally, the unsmoothed mean estimates $\hat{\phi}^{n}_{\alpha,j}$ are obtained from $\phi^{*,n}_{\alpha,p}$ using one of the two mean estimation methods elaborated in Section 3.2 – PIC or CIC. Let us define $\mathbf{K}_j$ to denote $\mathbf{I}_j$ (Eq. (21)) in case of the PIC scheme and $\mathbf{B}_j$ (Eq. (22)) in case of the CIC scheme. We now show that mean estimation given by Eq. (23) preserves the normalization condition:

$$\sum_{\alpha}\hat{\phi}_{\alpha,j} = \frac{\sum_p \mathbf{K}_j(\mathbf{x}_p) m^*_p c^*_p \sum_\alpha \phi^*_{\alpha,p}}{\sum_p \mathbf{K}_j(\mathbf{x}_p) m^*_p c^*_p} = 1. \tag{C.5}$$

Therefore, in summary, the numerical implementation of Eq. (98) satisfies realizability.

C.2. Conservation

We consider the conservation properties of the three numerical schemes – PIC-PC, CIC-LS and PIC-PL – for the case of a single scalar first. Conservation at the level of multiple species is addressed in Appendix C.2.3.

Consider the one-step update for the IEM mixing model given by Eq. (18) repeated here for convenience,

$$\phi^{*,n+1}_{p} = \phi^{*,n}_{p} + c^{*,n+\frac{1}{2}}_{p}\left(\tilde{\phi}^{*,n}_{p} - \phi^{*,n}_{p}\right) + \Delta\tilde{\phi}^{*,n+\frac{1}{2}}_{p},$$

where $\Delta\tilde{\phi}^{*,n+\frac{1}{2}}_{p}$ is the mean drift obtained using Eq. (A.15). Conservation requires that,

$$\sum_p m^*_p\left(\phi^{*,n+1}_{p} - \phi^{*,n}_{p}\right) = \sum_p m^*_p \Delta\tilde{\phi}^{*,n+\frac{1}{2}}_{p} + \sum_p m^*_p c^{*,n+1/2}_{p}\left(\tilde{\phi}^{*,n}_{p} - \phi^{*,n}_{p}\right) = 0. \tag{C.6}$$

It is therefore sufficient to satisfy the following:

$$\sum_p m^*_p \Delta\tilde{\phi}^{*,n+\frac{1}{2}}_{p} = 0, \tag{C.7}$$

$$\sum_p m^*_p c^{*,n+1/2}_{p}\tilde{\phi}^{*,n}_{p} = \sum_p m^*_p c^{*,n+1/2}_{p}\phi^{*,n}_{p} = 0. \tag{C.8}$$

The outline of this appendix is as follows. Since both the PIC-PC and the CIC-LS schemes are similar in mathematical form, we define $\mathbf{K}_j$ to denote $\mathbf{I}_j$ in case of the PIC-PC scheme and $\mathbf{B}_j$ in case of the CIC-LS scheme, as was done in Appendix C.1 and address the conservation properties of both these schemes in Appendix C.2.1 using $\mathbf{K}_j$. The PIC-PL scheme is dealt with in Appendix C.2.2 as an extension of the PIC-PC scheme. Finally, Appendix C.2.3 probes for detailed conservation with differential diffusion.

C.2.1. PIC-PC/CIC-LS

We consider the conservation properties of both the PIC-PS and CIC-LS schemes together in this section of Appendix C using $\mathbf{K}_j$ to denote $\mathbf{I}_j$ in case of the PIC-PC scheme and $\mathbf{B}_j$ in case of the CIC-LS scheme. Furthermore, conservation in terms of Eqs. (C.7) and (C.8) is considered separately.

We define the mass m_j of a cell centered at $\mathbf{x}_j$ to be,

$$m_j = \sum_p m^*_p \mathbf{K}_j(\mathbf{x}^*_p). \tag{C.9}$$

Now, consider Eq. (C.7), which can be re-expressed as,

$$\begin{aligned}\sum_p m^*_p \Delta\tilde{\phi}^{*,n+1/2}_{p} &= \sum_p m^*_p \sum_j \mathbf{K}_j\left(\mathbf{x}^*_p\right)\Delta\tilde{\phi}^{n+1/2}_{j},\\ &= \sum_j m_j \Delta\tilde{\phi}^{n+1/2}_{j}, \ = 0.\end{aligned} \tag{C.10}$$

The first line is obtained by using Eq. (27) to interpolate $\Delta\tilde{\phi}^{n+1/2}_{j}$ to particle locations. The second line comes by substituting m_j using Eq. (C.9). The last line is obtained due to the formulation of the Crank–Nicolson scheme given by Eq. (A.17). Thus, Eq. (C.7) is satisfied by both the PIC-PC and the CIC-LS schemes.

Next, we prove Eq. (C.8). Consider weights w to be defined as $w = mc$. Starting from the left-hand-side of Eq. (C.8) (and ignoring the time-levels for brevity), we obtain

$$\sum_p m_p^* c_p^* \tilde{\phi}_p^* = \sum_p w_p^* \tilde{\phi}_p^*,$$
$$= \sum_p w_p^* \sum_j \mathbf{K}_j\left(\mathbf{x}_p^*\right)\tilde{\phi}_j, \tag{C.11}$$
$$= \sum_j w_j \tilde{\phi}_j, \tag{C.12}$$

where the first line comes by using $w = mc$. The second line follows when interpolating $\tilde{\phi}_j$ to particle locations using Eq. (27) and the last line comes from Eq. (24). Note that $\tilde{\phi}_j$ is obtained by smoothing the unsmoothed estimates of the mean scalar $\hat{\phi}_j$ using weights w_j. As shown in Section 3.4.2, smoothing is conservative *i.e.*, $\sum_j w_j \tilde{\phi}_j = \sum_j w_j \hat{\phi}_j$ and therefore we can write,

$$\sum_p m_p^* c_p^* \tilde{\phi}_p^* = \sum_j w_j \hat{\phi}_j,$$
$$= \sum_j \sum_p \mathbf{K}_j\left(\mathbf{x}_p^*\right) w_p^* \phi_p^*,$$
$$= \sum_p w_p^* \phi_p^* = \sum_p m_p^* c_p^* \phi_p^*, \tag{C.13}$$

where the first line comes from using the conservation property of the smoothing operation. The second line follows from the mean estimation procedure given by Eq. (23) and third line comes because the summation of $\mathbf{K}_j$ over all j is unity. Thus we obtain the right hand side, showing that the PIC-PC/CIC-LS schemes are conservative.

C.2.2. PIC-PL

The conservation properties of the PIC-PL scheme are addressed in this section as an extension to the PIC-PC scheme. Given that the cell mass is defined by Eq. (C.9), with Eq. (28) the left hand side of Eq. (C.7) becomes,

$$\sum_p m_p^* \Delta\tilde{\phi}_p^* = \sum_p m_p^* \sum_j \mathbf{I}_j\left(\mathbf{x}_p^*\right)\Delta\tilde{\phi}_j + \zeta \sum_p m_p^* \sum_j \mathbf{I}_j\left(\mathbf{x}_p^*\right)\left(\mathbf{x}_p^* - \bar{\mathbf{x}}_j^{\Delta}\right).\boldsymbol{v}_j^{\Delta},$$
$$= \sum_p m_p^* \sum_j \mathbf{I}_j\left(\mathbf{x}_p^*\right)\Delta\tilde{\phi}_j \tag{C.14}$$

by the definition of $\bar{\mathbf{x}}_j^{\Delta}$ given by,

$$\bar{\mathbf{x}}_j^{\Delta} = \frac{\sum_p \mathbf{I}_j\left(\mathbf{x}_p^*\right) m_p^* \mathbf{x}_p^*}{\sum_p \mathbf{I}_j(\mathbf{x}_p^*) m_p^*} \tag{C.15}$$

and $\boldsymbol{v}_j^{\Delta} = \mathbf{e}_k \delta_k \Delta\tilde{\phi}_j$ is an approximation to $\nabla\Delta\tilde{\phi}_j$. As shown in Appendix C.2.1,

$$\sum_p m_p^* \sum_j \mathbf{I}_j\left(\mathbf{x}_p^*\right)\Delta\tilde{\phi}_j = 0.$$

Next we consider Eq. (C.8) for the PIC-PL scheme. Using Eq. (28), the left hand side of Eq. (C.8) is written as,

$$\sum_p m_p^* c_p^* \tilde{\phi}_p^* = \sum_p m_p^* c_p^* \sum_j \mathbf{I}_j\left(\mathbf{x}_p^*\right)\tilde{\phi}_j + \zeta \sum_p m_p^* c_p^* \sum_j \mathbf{I}_j\left(\mathbf{x}_p^*\right)\left(\mathbf{x}_p^* - \bar{\mathbf{x}}_j\right)v_j, \tag{C.16}$$
$$= \sum_p m_p^* c_p^* \sum_j \mathbf{I}_j\left(\mathbf{x}_p^*\right)\tilde{\phi}_j \tag{C.17}$$

by the definition of $\bar{\mathbf{x}}_j$ which is given by,

$$\bar{\mathbf{x}}_j = \frac{\sum_p \mathbf{I}_j(\mathbf{x}_p^*) m_p^* c_p^* \mathbf{x}_p^*}{\sum_p \mathbf{I}_j(\mathbf{x}_p^*) m_p^* c_p^*}. \tag{C.18}$$

As shown in Appendix C.2.1,

$$\sum_p m_p^* c_p^* \sum_j \mathbf{I}_j\left(\mathbf{x}_p^*\right)\tilde{\phi}_j = \sum_p m_p^* c_p^* \phi_p^{*,n}.$$

This shows that the PIC-PL scheme is also conservative.

C.2.3. Multiple species with unequal diffusivities

While considering multiple species each with different diffusivity, conservation requires that

$$\sum_p m_p^* \Delta\tilde{\phi}_{\alpha,p}^{*,n+\frac{1}{2}} = 0, \tag{C.19}$$

where $\Delta\tilde{\phi}_{\alpha,p}^{*,n+\frac{1}{2}}$ is obtained by interpolating $\Delta\tilde{\phi}_{\alpha,j}^{n+\frac{1}{2}}$ given by Eq. (A.38) to particle locations. Eq. (A.40) suggests that conservation is satisfied at the cell level. Since interpolation from estimates at the cell level to particle locations satisfies conservation criterion, we conclude that detailed conservation is satisfied in the case of multiple species with different diffusivities.

In summary, Appendix C presents evidence to show that the numerical implementation detailed in Section 3 satisfies conservation and realizability.

Appendix D. Description of tests

The formulations of test cases using the Method of Manufactured Solutions are described here in the following two subsections. Appendix D.1 details the constant-density test case in a Cartesian coordinate system, and Appendix D.2 provides specifications for the test problem in a cylindrical system.

D.1. Cartesian system

The manufactured solutions used in this work are defined in terms of several constants which are ascribed the values:

$$\begin{aligned} &\omega = \frac{10}{2\pi},\ L = 2\pi,\ \phi_{m,o} = \frac{1}{45},\ \phi_{v,o} = \frac{1}{125},\ \Omega_o = \frac{1}{2}, \\ &D_o = \frac{1}{4},\ D_{o,t} = \frac{4}{5},\ U_o = 1,\ R_o = 1,\ J_o = 1. \end{aligned} \tag{D.1}$$

Given the constants above, the manufactured solutions to Eqs. (65) and (66) are specified as functions of the three spatial coordinates x, y and z in a 3D Cartesian coordinate system and time t:

$$\bar{\phi}_m = \phi_{m,o} e^{4\omega t}(\cos(x) + \cos(z) + \sin(y) + 4), \tag{D.2}$$

$$\overline{\phi'^2}_m = \phi_{v,o}(4 - e^{-3\omega t})(\cos(y) + \sin(x) + \sin(z) + 4), \tag{D.3}$$

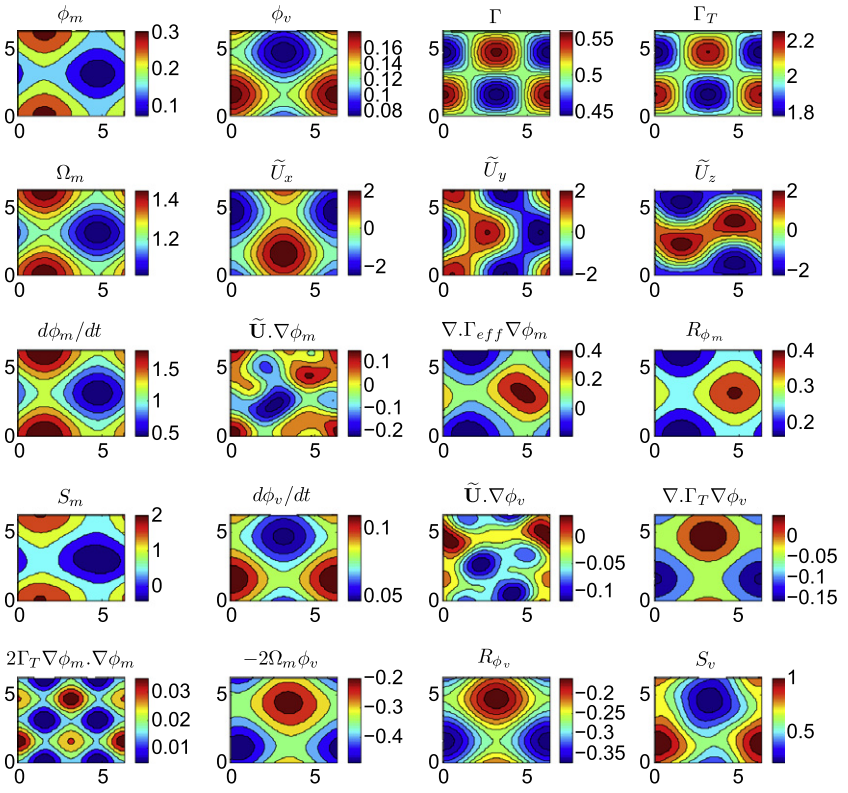

Fig. D.24. Contour plots of the various MMS quantities in y–z plane at $x = 0.4L$ and $\omega t = 0.25$.

respectively where $\{x,y,z\} \in [0 \quad L]$ and $\omega t \in [0 \quad 1]$. The second moment is then obtained as a sum of the variance and the square of the mean. The effective diffusivity $\Gamma_{\text{eff}} = \Gamma + \Gamma_T$, sub-grid scale turbulent diffusivity Γ_T and molecular diffusivity Γ are given by,

$$\Gamma_{\text{eff}} = D_{\text{o}}\left(e^{-4\omega t} + \frac{e^{4\omega t}}{20}\right)(4\cos(y)\sin(x)\sin(z) - 4 + 24), \tag{D.4}$$

$$\Gamma_T = D_{\text{o,t}}\Gamma_{\text{eff}}, \tag{D.5}$$

$$\Gamma = (1 - D_{\text{o,t}})\Gamma_{\text{eff}}. \tag{D.6}$$

Finally, the mixing frequency Ω_m and velocity $\tilde{\mathbf{U}}$ as given below,

$$\Omega_m = -\frac{2\Omega_{\text{o}}\left(\cos\left(\pi\omega\left(2t - \frac{1}{5}\right)\right) + \frac{6}{5}\right)\left(\cos(z) + \sin(x) + \sin(y) + \frac{51}{5}\right)}{5(e^{-3\omega t} - 4)}, \tag{D.7}$$

$$\tilde{U}_x = U_{\text{o}}\left(\frac{4}{e^{4\omega t}} + \frac{e^{4\omega t}}{10}\right)(\cos(x)\cos(y) + \sin(x)\sin(z)), \tag{D.8}$$

$$\tilde{U}_y = U_{\text{o}}\left(\frac{4}{e^{4\omega t}} + \frac{e^{4\omega t}}{10}\right)(\cos(y)\cos(z) + \sin(x)\sin(y)), \tag{D.9}$$

$$\tilde{U}_z = U_{\text{o}}\left(\frac{4}{e^{4\omega t}} + \frac{e^{4\omega t}}{10}\right)(\cos(x)\cos(z) + \sin(y)\sin(z)), \tag{D.10}$$

and the source terms S_m and S_v can be obtained from Eqs. (65) and (66), respectively.

Fig. D.24 plots the contours of various quantities at $x = 0.4L$ and $\omega t = 0.25$.

D.2. Cylindrical system

In the cylindrical coordinate system, the manufactured solutions are defined in terms of several constants that are ascribed the following values:

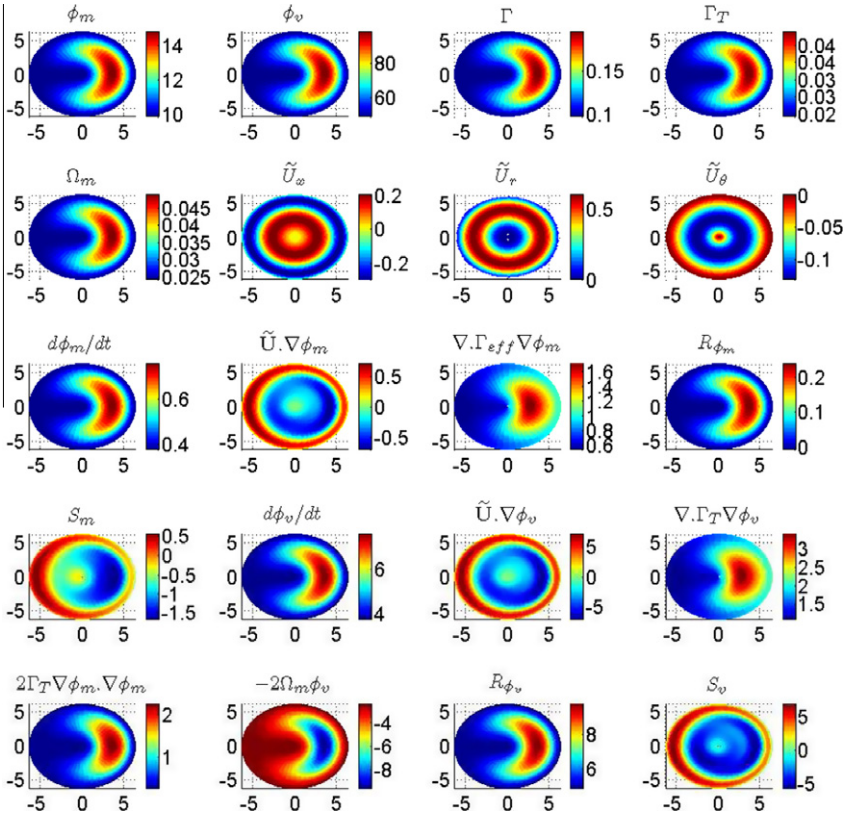

Fig. D.25. Contour plots of the various MMS quantities in r–θ plane at $x = 0.4L$ and $\omega t = 0.5$

$$\omega = \frac{1}{4\pi},\ L = 2\pi,\ \phi_{m,o} = 2,\ \phi_{v,o} = 200,\ \Omega_o = \frac{2}{100},$$
$$D_o = \frac{5}{100},\ D_{o,t} = \frac{2}{10},\ U_o = -\frac{2}{100},\ R_o = -\frac{5}{100},\ J_o = 10. \tag{D.11}$$

The manufactured solutions to Eqs. (65) and (66) are specified as,

$$\bar{\phi}_m = \frac{\phi_{m,o}(\cos(x)+2)\left(r^2(\cos(\theta)+1)\left(\cos\left(\frac{r}{2}\right)+1\right)+20\right)\left(e^{-5\omega t}+\frac{e^{5\omega t}}{100}\right)}{2} + 5, \tag{D.12}$$

$$\overline{\phi'^2}_m = \frac{\phi_{v,o}(\cos(x)+2)\left(r^2(\cos(\theta)+1)\left(\cos\left(\frac{r}{2}\right)+1\right)+20\right)\left(e^{-5\omega t}+\frac{e^{5\omega t}}{100}\right)}{20} + \frac{1571}{5000}, \tag{D.13}$$

respectively where $\{x, r, \theta\} \in [0 \quad L]$ and $\omega t \in [0 \quad 1]$. The other properties and the velocity field are given by,

$$\Gamma_{\text{eff}} = \frac{D_o(\cos(x)+2)\left(r^2(\cos(\theta)+1)\left(\cos\left(\frac{r}{2}\right)+1\right)+20\right)\left(e^{-5\omega t}+\frac{e^{5\omega t}}{100}\right)}{2}, \tag{D.14}$$

$$\Omega_m = \frac{\Omega_o(\cos(x)+2)\left(r^2(\cos(\theta)+1)\left(\cos\left(\frac{r}{2}\right)+1\right)+20\right)\left(e^{-5\omega t}+\frac{e^{5\omega t}}{100}\right)}{4}, \tag{D.15}$$

$$\widetilde{U}_x = U_o \sin(x)\left(\frac{r^3 \sin\left(\frac{r}{2}\right)}{2} - 3r^2\left(\cos\left(\frac{r}{2}\right)+1\right)\right), \tag{D.16}$$

$$\widetilde{U}_r = U_o r^3 \cos(x)\left(\cos\left(\frac{r}{2}\right)+1\right), \tag{D.17}$$

$$\widetilde{U}_\theta = 2U_o r\left(\cos\left(\frac{r}{2}\right)+1\right). \tag{D.18}$$

The sub-grid scale diffusivity, Γ_T and molecular diffusivity Γ are obtained using Eqs. (D.5 and D.6) respectively and the source terms S_m and S_v can be obtained from Eqs. (65) and (66), respectively.

The contours of various quantities at $x = 0.4L$ and $\omega t = 0.5$ are plotted in Fig. D.25.

References

[1] R.W. Bilger, S.B. Pope, K.N.C. Bray, J.F. Driscoll, Paradigms in turbulent combustion research, Proc. Combust. Inst. 30 (2005) 21–42.
[2] R.S. Cant, E. Mastorakos, An introduction to turbulent reacting flows, Imperial College Press, London, 2008.
[3] R. Sankaran, E.R. Hawkes, J.H. Chen, T. Lu, C.K. Law, Structure of a spatially developing turbulent lean methane-air bunsen flame, Proc. Combust. Inst. 31 (1) (2007) 1291–1298.
[4] S.B. Pope, Turbulent flows, Cambridge University Press, Cambridge, 2000.
[5] H. Pitsch, Large-eddy simulation of turbulent combustion, Annu. Rev. Fluid Mech. 38 (2006) 453–482.
[6] P. Sagaut, Large eddy simulation for incompressible flows, Springer, Berlin, 2006.
[7] S.B. Pope, PDF methods for turbulent reactive flows, Prog. Energy Combust. Sci. 11 (1985) 119–192.
[8] S.B. Pope, Computations of turbulent combustion: Progress and challenges, Proc. Combust. Inst. 23 (1990) 591–612.
[9] D.C. Haworth, Progress in probability density function methods for turbulent reacting flows, Prog. Energy Combust. Sc. 36 (2010) 168–259.
[10] F. Gao, E.E. O'Brien, A large-eddy simulation scheme for turbulent reacting nows, Phys. Fluids A 5 (1993) 1282–1284.
[11] P.J. Colucci, F.A. Jaberi, P. Givi, S.B. Pope, Filtered density function for large eddy simulation of turbulent reacting nows, Phys. Fluids 10 (2) (1998) 499–515.
[12] F.A. Jaberi, P.J. Colucci, S. James, P. Givi, S.B. Pope, Filtered mass density function for large-eddy simulation of turbulent reacting nows, J. Fluid Mech. 401 (1999) 85–121.
[13] S.B. Pope, Self-conditioned fields for large-eddy simulations of turbulent flows, J. Fluid Mech. 652 (2010) 139–169.
[14] J. Villermaux, J.C. Devillon, Représentation de la coalescence et de la redispersion des domaines de ségrégation dans un fluide par un modèle d'interaction phénoménologique, Proc. of the 2nd Int. Symp. on Chem. React. Eng, 26, Elsevier, New York, 1972, pp. 1–13.
[15] C. Dopazo, E.E. O'Brien, An approach to the autoignition of a turbulent mixture, Acta Astronaut. 1 (1974) 1239–1266.
[16] S.B. Pope, On the relationship between stochastic Lagrangian models of turbulence and second-moment closures, Phys. Fluids 6 (1994) 973–985.
[17] R.O. Fox, On velocity conditioned scalar mixing in homogeneous turbulence, Phys. Fluids 8 (1996) 2678–2691.
[18] S. Subramaniam, S.B. Pope, A mixing model for turbulent reactive flows based on Euclidean minimum spanning trees, Combust. Flame 115 (1998) 487–514.
[19] R.L. Curl, Dispersed phase mixing I: Theory and effects in simple reactors, AIChE J. 9 (2) (1963) 175–181.
[20] C. Dopazo, Relaxation of initial probability density function in the turbulent convection of scalar nelds, Phys. Fluids 22 (1979) 20–30.
[21] J. Janicka, W. Kolbe, W. Kollmann, Closure of the transport equation for the probability density function of turbulent scalar nelds, J. Non-Equilib. Thermodyn. 4 (1979) 47–66.
[22] S.B. Pope, An improved turbulent mixing model, Combust. Sci. Technol. 28 (1982) 131–145.
[23] A.Y. Klimenko, S.B. Pope, A model for turbulent reactive flows based on multiple mapping conditioning, Phys. Fluids 15 (2003) 1907–1925.
[24] M.J. Cleary, A.Y. Klimenko, A generalized multiple mappling conditioning approach for turbulent comsbution, Flow, Turbul. Combust. 82 (2009) 477–491.
[25] R. Cao, H. Wang, S.B. Pope, The effect of mixing models in PDF calculations of piloted jet flames, Proc. Combust. Inst. 31 (2007) 1543–1550.
[26] S. Mitarai, J.J. Riley, G. Kosaly, Testing of mixing models for Monte Carlo probability density function simulations, Phys. Fluids 17 (2005) 047101–047115.
[27] S.B. Pope, The relationship between the probability approach and particle models for reaction in homogeneous turbulence, Combust. Flame 35 (1979) 41–45.
[28] M.S. Anand, S.B. Pope, Diffusion behind line source in grid turbulence, Turbul. Shear Flows 4 (1985) 46–61.

[29] R. McDermott, S.B. Pope, A particle formulation for treating differential diffusion in filtered density function methods, J. Comput. Phys. 226 (1) (2007) 947–993.
[30] K.A. Kemenov, S.B. Pope, Molecular diffusion effects in LES of a piloted methane-air flame, Combust. Flame 158 (2011) 240–254.
[31] H. Wang, S.B. Pope, Large eddy simulation/probability density function modeling of a turbulent $CH_4/H_2/N_2$ jet flame, Proc. Combust. Inst. 33 (2011) 1319–1330.
[32] V. Raman, H. Pitsch, A consistent LES/filtered density function formulation for the simulation of turbulent flames with detailed chemistry, Proc. Combust. Inst. 31 (2007) 1711–1719.
[33] J. Xu, S.B. Pope, Assessment of numerical accuracy of PDF/Monte Carlo methods for turbulent reactive flows, J. Comput. Phys. 152 (1999) 192–230.
[34] P. Jenny, S.B. Pope, M. Muradoglu, D.A. Caughey, A hybrid algorithm for the joint PDF equation for turbulent reactive flows, J. Comput. Phys. 166 (2001) 252–281.
[35] M. Muradoglu, K. Liu, S.B. Pope, PDF modeling of a bluff-body stabilized turbulent flame, Combust. Flame 132 (2003) 115–137.
[36] M. Muradoglu, S.B. Pope, D.A. Caughey, The hybrid method for the PDF equations of turbulent reactive flows: consistency conditions and correction algorithms, J. Comput. Phys. 172 (2001) 841–878.
[37] H. Wang, S.B. Pope, Time averaging strategies in the finite-volume/particle hybrid algorithm for the joint PDF equation of turbulent reactive flows, Combust. Theory Model. 12 (3) (2008) 529–544.
[38] H. Wang, P.P. Popov, S.B. Pope, Weak second order splitting schemes for Lagrangian Monte Carlo particle methods for the composition PDF/FDF transport equations, J. Comput. Phys. 229 (2010) 1852–1878.
[39] P.J. Roache, Code verincation by the method of manufactured solutions, J. of Fluids Eng. 124 (1) (2002) 4–10.
[40] C.J. Roy, Review of code and solution verincation procedures for computational simulation, J. Comput. Phys. 205 (2005) 131–156.
[41] C.J. Roy, C.C. Nelson, T.M. Smith, C.C. Ober, Verincation of Euler/Navier-Stokes codes using the method of manufactured solutions, Int. J. for Numerical Methods in Fluids 44 (2004) 599–620.
[42] L. Eça, M. Hoekstra, A. Hay, D. Pelletier, Verincation of RANS solvers with manufactured solutions, Eng. Comput. 23 (2007) 253–270.
[43] J.C. Sutherland, P.J. Smith, J.H. Chen, Quantification of differential diffusion in nonpremixed systems, Combust. Theory Model. 9 (2) (2005) 365–383.
[44] E.S. Oran, J.P. Boris, Detailed modelling of combustion systems, Prog. Energy Combust. Sc. 7 (1) (1981) 1–72.
[45] T.P. Coffee, J.M. Heimerl, Transport algorithms for premixed, laminar steady-state flames, Combust. Flame 43 (1981) 273–289.